

Rotor effective wind field estimation and multi-body dynamic characterization of a 45 kW horizontal axis wind turbine

Downloaded from: https://research.chalmers.se, 2025-10-18 21:41 UTC

Citation for the original published paper (version of record):

Panda, D., Chakraborty, A., Sarkar, S. et al (2026). Rotor effective wind field estimation and multi-body dynamic characterization of a 45 kW horizontal axis wind turbine. Renewable Energy, 256. http://dx.doi.org/10.1016/j.renene.2025.124343

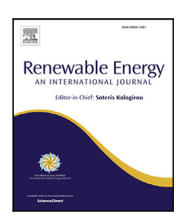
N.B. When citing this work, cite the original published paper.

research.chalmers.se offers the possibility of retrieving research publications produced at Chalmers University of Technology. It covers all kind of research output: articles, dissertations, conference papers, reports etc. since 2004. research.chalmers.se is administrated and maintained by Chalmers Library

Contents lists available at ScienceDirect

Renewable Energy

journal homepage: www.elsevier.com/locate/renene



Rotor effective wind field estimation and multi-body dynamic characterization of a 45 kW horizontal axis wind turbine

Debasis Panda ^a, Arunasis Chakraborty ^a, Saptarshi Sarkar ^c, Håkan Johansson ^b

- ^a Department of Civil Engineering, Indian Institute of Technology Guwahati, Assam, India
- b Department of Mechanical and Maritime Sciences, Chalmers University of Technology, Gothenburg, Sweden
- ^c Department of Electrification and Reliability, RISE Research Institutes of Sweden AB, Gothenburg, Sweden

ARTICLE INFO

Keywords: Horizontal Axis Wind Turbine Multibody dynamics Extended Kalman filter Wind field estimation Modal identification

ABSTRACT

This paper presents inverse systems identification of a horizontal axis wind turbine to bench-mark the complete multi-body system. This is achieved by an extended Kalman-based time marching algorithm of a rotor-effective wind flow model involving rotor speed, generator torque, and power output. In addition to wind estimation, comprehensive inverse characterization of the turbine is also presented here. For this purpose, the dynamic characterization of a unique wooden tower is considered first, followed by the detailed aeroelastic characterization of the blades made of carbon fiber using a series of tests and detailed modeling. The tower and blade root measurements are utilized to identify in situ modal characteristics, further validating the model and its performance. Finally, the steady-state response of the tower and blade at different mean wind speeds is identified for complete bench-marking. The numerical results presented in this article highlight the accuracy of the proposed wind estimation and the characterization of the close-loop system under different operating conditions.

1. Introduction

The worldwide wind energy landscape is driven by innovation, advancement, and a never-ending pursuit of increased efficiency. With the surging deployment of Horizontal Axis Wind Turbines (HAWTs), whether in utility-scale land-based projects or offshore ventures, the quest for optimal and sustainable performance continues to drive this sector. The accomplishment of these goals in achieving the full potential of wind power depends on sophisticated modeling and control systems combined with inverse characterization and continuous monitoring techniques. This path towards improved control and optimization requires high-fidelity multi-body dynamic models, which offer invaluable insights into the behavior of HAWTs, enabling researchers and engineers to fine-tune their performance and accurately predict loads for estimating fatigue life. In this context, the need for benchmark models, particularly for small-scale HAWTs, is one of the most apparent obstacles in this path to precision. Benchmark models are essential tools for thorough analysis, allowing for standardized comparisons and control strategy optimization. They serve as the foundation for innovation and are an indispensable tool for overcoming the challenges of wind turbine scaling, whether for onshore or offshore usage.

In the realm of large-scale wind turbines, theoretical benchmark models are abundant, e.g., the renowned NREL 5 MW baseline model $\frac{1}{2}$

[1], DTU 10 MW [2] and International Energy Agency 15 MW model [3] stand as a testament to their importance. However, ramifications of scaling wind turbines to different sizes in terms of both loads and turbine output, it is necessary to have a collection of similar wind turbine models of varying sizes. The Wind Partnership for Advanced Component Technologies (WindPACT) program, initiated by the NREL, charted the way by developing four baseline wind turbine models with varying power ratings. 750 kW, 1.5 MW, 3 MW, and 5 MW [4]. These models were originally implemented in FAST, (i.e., Fatigue, Aerodynamics, Structures, and Turbulence) [5], which is a popular aeroelastic code for simulating onshore and offshore wind turbines.

These benchmark models have become invaluable tools for comparative studies in wind turbine research. They provide standardized platforms for evaluating dynamic responses and validating simulation frameworks, enabling effective load estimation strategies under varying environmental and fault conditions. Rezaei et al. [6] developed a complete multibody model of the NREL 5 MW turbine, which incorporates geometric nonlinearities to analyze rotor dynamics and flutter instabilities and highlighted the importance of full-system modeling compared to simplified approaches. Similarly, Xue et al. [7] explored the rigid–flexible coupling of the 5 MW wind turbine under elevated wind conditions, providing guidelines for structural improve-

E-mail address: saptarshi.sarkar@ri.se (S. Sarkar).

^{*} Corresponding author.

ments based on the dynamic responses. Mitra et al. [8] utilized a high-fidelity aero-servo-elastic model to optimize the composite blade fiber orientation and demonstrated how bending-torsion coupling influences both control response and aerodynamic efficiency of wind turbines. Additionally, Liu et al. [9] studied the wake dynamics of the offshore 5 MW turbine using large eddy simulations and actuator line modeling under varying inflow turbulence conditions. According to their research, higher turbulence speeds up the wake recovery, which enhances energy extraction for downstream wind turbines. In addition to modeling, benchmark turbines play a vital role in the development and testing of advanced control algorithms to enhance performance and minimize structural loads. Sarkar and Chakraborty [10] introduced a semi-active vibration control strategy that employs multiple magnetorheological tuned liquid column dampers on a wind turbine tower. This approach demonstrated the effectiveness of magnetorheological devices in providing adaptive damping under varying wind loads. Further, Abdelbaky et al. [11] developed a partially offline fuzzy logic-based model-predictive control for pitch regulation of the NREL 5 MW turbine. This method successfully addresses pitch actuator saturation and outperforms traditional proportional-integral (PI) controllers. A multi-resolution wavelet-based LOR controller was proposed by Sarkar et al. [12] for individual pitch control of floating offshore wind turbines, demonstrating improved mitigation of blade and tower vibrations under combined wind-wave-current conditions by emphasizing frequency band-specific dynamics. Hu et al. [13] implemented a modular open-source baseline controller for the DTU 10 MW wind turbine on a Tension Leg Platform (TLP) using FAST. They compared conventional pitch-to-feather and active pitch-to-stall strategies, showing how control frequency tuning affects rotor dynamics, platform stability, and thrust-induced responses under extreme offshore conditions. In the context of fatigue and reliability, Sajeer et al. [14] used a spinning finite element model to investigate the role of longitudinal stiffeners in improving the fatigue life of the 5 MW turbine blade. Their findings provide structural enhancement strategies based on dynamic loading patterns. Yang et al. [15] studied the failure of tendons in a floating 10 MW turbine, showcasing the significance of controller robustness during fault scenarios. The emerging 15 MW class turbines, in particular, present significant difficulties because of their unparalleled size and flexibility. Chai et al. [16] examined extreme wave and wind events for the IEA 15 MW turbine, underlining the need for robust modeling and control. Further, Liang et al. [17] emphasized the importance of scalable control and monitoring frameworks, as larger rotors introduce stronger aeroelastic effects and demand more robust load mitigation strategies.

Moreover, for small-scale turbines, such benchmark models are rare, without any in-depth analysis and the refinement of control techniques for this specific type. This dearth underscores a significant gap in our understanding of these smaller, often more localized wind energy solutions installed in large numbers. To this end, IEA Wind Task 27 [18], titled Small Wind Turbines in Turbulent Sites, aims to enhance the understanding of how turbulence impacts the performance and reliability of small wind turbines, particularly in complex terrain and urban environments. Its objectives include developing standardized methods for measuring turbulence, evaluating its effects on turbine performance and structural integrity, and fostering international collaboration to share data and best practices. Meanwhile, IEA Wind Task 41 [19], Enabling Wind to Contribute to a Sustainable Future Energy System, focuses on supporting the integration of wind energy into future energy systems. It seeks to analyze the role of wind in decarbonization, develop tools for system integration, such as storage and grid flexibility, and facilitate knowledge exchange on policy and market design to promote the growth of wind energy. Both tasks contribute to understanding the performance and reliability of small wind turbines. In this context, the paper serves two purposes: firstly, to benchmark a small wind turbine against field data, and secondly, to perform inverse identification of the dynamics of a wooden wind turbine tower. The wooden tower is a

unique technology that offers a significantly lower net-carbon-emission alternative to traditional steel towers.

Traditionally, the inverse problem is solved in two major paradigms. In one approach, the measured response time histories are analyzed using signal processing tools to identify fundamental structural dynamic parameters. This approach is easy to implement and provides fast-hand information necessary for model verification. However, output-only signal processing-based modal identification may face difficulty as the measured responses often contain the rotational frequency of the turbine and its harmonics, which are difficult to segregate from structural frequencies. On the other hand, the second approach adopts a model whose parameters are updated using filtering algorithms. They are often sensitive to modeling inaccuracies and require well-defined noise statistics. Both these approaches have their pros and cons, which are highlighted below. In recent years, wavelet analysis has become more well-known in system identification due to its superior time-frequency analysis capabilities and aptitude for handling non-stationary data. It offers a distinct viewpoint by presenting the modulus of wavelet transforms, often visualized as scalograms, in a time-frequency plane. The wavelet coefficients exhibit maximum values at the instantaneous frequency, corresponding to the dominant structural frequencies in the signal at that instant of time [20,21]. This property allows wavelet analysis to discern the critical modal parameters of the system accurately. Several studies have been made for extracting the natural frequency and damping properties [22,23] because of its inherent advantages. Some notable studies have explored the potential of wavelet analysis in connection with wind turbines. For instance, Murtagh and Basu [24] introduced two approaches to evaluate the equivalent modal viscous damping ratios for a wind turbine tower. The first method is based on the Fourier transformation of the motion equation, using the least square method to estimate the equivalent viscous damping ratios. The second method utilizes the wavelet transformation, employing a timesegmented least square approach to extract the damping ratios. For identifying time-variant aerodynamic damping matrices of wind turbines, Chen et al. [25] put forth a methodology using a wavelet-based equivalent linearization technique. Some studies have explored the potential of wavelet-based analysis to identify faults in wind turbines. Complex wavelet transform has been utilized to uncover weak bearing fault signatures suppressed by dominant gear vibrations, particularly in gearboxes with coexisting faults [26]. In parallel, advanced timefrequency techniques like the reassigned second-order synchrosqueezing transform have been introduced to accurately capture time-varying fault features in variable-speed operations, demonstrating improved clarity in fault characterization [27]. Further, continuous wavelet transforms for LQR-based gain scheduling, optimizing fore-aft vibration control in horizontal axis wind turbine towers were examined by Mitra et al. [28]. However, there is a significant gap in the research regarding identifying critical modal parameters utilizing measurements from wind turbines and validating these findings against actual models.

Model-based methods, on the other hand, use filtering techniques to recursively update a dynamic model in order to estimate unknown loads or system characteristics. Variants of the Kalman filter have been widely used in this field. Schlipf and Cheng [29] used an Extended Kalman Filter (EKF) to demonstrate that wind turbine states and inflow conditions could be estimated reliably. Using limited sensor response data, an augmented Kalman filter (AKF) was used by [30] to estimate unbalanced rotor loads in spinning machinery. Lei et al. [31] extended the EKF framework to use under ambient excitations for identifying structural element mass and stiffness changes in chain-like systems using acceleration data. Similarly, Wei et al. [32] proposed a Kalman filter-based approach combining structural acceleration data with BeiDou satellite measurements to estimate tower-top thrust and distributed bending moments in a full-scale 2.5 MW wind turbine. More recently, hybrid estimation frameworks have emerged to leverage the advantages of both physics-based and data-driven methods. For instance, Mehrjoo et al. [33] developed a surrogate input load estimation

model combining transfer learning and multitask learning, enabling real-time load predictions in offshore wind turbines while addressing limitations of traditional model fidelity and data availability. While model-based and hybrid techniques have appealing capabilities, such as real-time performance and robustness under uncertain conditions, they are often sensitive to modeling inaccuracies and require well-defined noise statistics. In contrast, signal-based methods like the wavelet-based framework presented in this study provide a flexible and data-centric route for extracting dynamic characteristics from full-scale turbine measurements. The identified modal parameters are further validated using a high-fidelity finite element model to demonstrate the accuracy and applicability of the proposed methodology.

Besides model identification, wind field characterization is key to the successful inverse modeling of any multi-body wind turbine system, especially with variable pitch rotors acting in a close loop. The wind speed measurements obtained from the standard anemometer at the top of a wind turbine lack the requisite accuracy for high-fidelity analyses. Thus, rotor effective wind speed estimation in modern turbines is the prerequisite for designing advanced control strategies, condition assessment, power estimation, and downtime regulation. It involves various state estimation techniques that have been explored in the literature. For example, Kalman filters and their advanced variants were adopted in [34] to estimate the rotor-effective wind speed. The wind speed estimators were designed using a single-state observer for a simplified turbine model. Another approach explained in [35] employed a state observer to estimate aerodynamic torque. Subsequently, the effective wind speed was estimated based on the torque estimate through the inversion of the aerodynamic torque model. Besides rotor effective wind speed, aerodynamic torque estimation in the presence of close loop control is also essential. It helps to characterize the realistic power output of a turbine operating in a turbulent environment. Comprehensive surveys and comparisons of rotor-effective wind speed estimation methods using different state estimation techniques may be found in [36]. Based on measured turbine responses such as rotor speed and power produced, an effective wind speed, representing the wind field averaged over the rotor disc, was proposed in [37]. This effective wind speed estimator is based on an Extended Kalman Filter (EKF), which leverages nonlinear time-varying turbulence models. Furthermore, in the ROSCO model [38], the wind speed estimator from [37] was utilized for the TSR tracking generator torque controller and to set pitch saturation routines. A data-driven framework was proposed for real-time estimation of rotor effective wind speed by combining Gaussian process regression with an extended Kalman filter. This approach eliminates the need for precomputed aerodynamic maps by learning the surface of the power coefficient directly from realtime measurements, enabling accurate estimation of REWS even under down-regulated conditions [39]. Despite its improved accuracy, the proposed method relies on a regression model trained from limited simulation data, which can reduce accuracy under highly unanticipated or unmodeled operating conditions.

Recently, light detection and ranging (LiDAR) [40] technology has gained traction in wind energy applications due to its ability to provide more accurate rotor-aligned wind measurements, enhancing the accuracy of turbine response analysis and control strategies. Doppler LiDAR scanning has been investigated to reconstruct the site-specific wind profiles up to 500 m, allowing detailed response analysis of large offshore wind turbines such as the 10 MW and 15 MW models [41]. Similarly, a minute-scale prediction framework has been proposed using limited LiDAR data and transfer learning, showing improved forecasting of incoming wind conditions, but still heavily depends on previously acquired data, reducing its adaptability to evolving sites [42]. On the control side, uncertainty-aware LiDAR models compatible with robust control techniques like μ -synthesis and Quantitative Feedback Theory (QFT) have been proposed in [43], but they demand approximations of nonlinear sensor dynamics in linear uncertainty sets, which can

compromise accuracy under fluctuating conditions. Despite their potential, LiDAR-based solutions for wind turbine monitoring and control are still in the early adoption phase, with high implementation costs limiting their large-scale deployment in operational wind farms. In general, using measurements such as rotor speed, generator torque, and other controller inputs, an EKF-based state observer coupled with a wind flow model can effectively estimate rotor-effective wind speed to tune the critical performance matrices of an operating wind turbine. The effectiveness of these models in replicating real-world scenarios through complete aeroelastic simulations and validating them with actual test data has not been attempted earlier but is addressed in this work. This approach offers a practical and cost-effective solution and can be a promising alternative to improve wind turbine performance and control strategies under varying conditions.

1.1. Objectives

The literature review presented above outlines the demand for benchmark reference models of HAWT, especially for small-scale turbines. Most of the benchmark models reported in the literature are hypothetical. Only a limited number of benchmark models are available in the public domain. To address this issue, a horizontal axis test turbine at Björkö, Sweden, provides necessary data for various response characterizations under different operating conditions. Modeling this turbine and validating it with actual test data involves parameter estimation from the actual measurements, which is the key objective of this study. Thus, the deliverables of this work are outlined below.

- System characterization of a test turbine, which includes extraction of the structural properties and other parameters of the tower and blade through detailed analysis and signal processing-based model validation using field measurements.
- Rotor effective wind field characterization through inverse analysis of actual measurements using an Extended Kalman Filteringbased wind flow model identification to replicate the actual operating scenarios of the test turbine through high-fidelity model simulation.
- Validation of the detailed multi-body system by comparing different response quantities obtained through the complete aeroelastic simulation of the turbine using an OpenFAST model over the complete operating range of the turbine.

Further, this paper is organized as follows. Section 2 provides a comprehensive description of the test turbine, starting with the general characteristics, followed by the extraction of structural properties from testing and finally, a modal description of the tower and blade. It also describes the driven train properties along with other relevant parameters necessary for detailed modeling. The turbine's control systems are described in Section 3, and the control parameters for the desired power output are listed. Section 4 documents the sensor and measurement details of the test turbine. In Section 5, the inverse analysis of measurements is conducted in two phases. Initially, modal parameters are extracted through signal processing, with wavelet-based time-frequency analysis as the primary tool. Once these modal parameters are identified, a meaningful comparison for benchmark demands wind field characterization. To address this issue, the rotor effective wind speed is estimated using an EKF-based model updating technique to tune the simulated turbine responses with field measurements. Then, in Section 6, different simulated responses of the updated aeroelastic model in OpenFAST [44] are validated against the test data. Further, an analysis of the steady-state responses of the tower and blades is included, demonstrating their behavior as functions of wind speeds. Finally, conclusions are drawn in Section 7.



Fig. 1. Chalmers wind turbine and its components: (a) Geographic coordinate, (b) Rotor Nacelle Assembly (RNA), (c) Steel top adopter, (d) CAD model of wooden tower body, (e) CAD model of Steel base.

2. General description of the test turbine

This study uses an onshore horizontal axis wind turbine located on Björkö Island, approximately 20 km west of Göteborg City, Sweden. The turbine was erected in 2020 with the support of the Swedish Wind Power Technology Centre, the Swedish Energy Agency, and Region Västra Götaland, to facilitate research in wind energy. The coordinates are: 57.71818820625921, 11.683382148764485. The novelty of this wind turbine is its tower, which is made of wood laminates. The blades are made of carbon fiber, hence they are lighter and stiffer compared to traditional blade materials. Some critical components of this turbine are shown in Fig. 1. The tower begins with a concrete foundation upon which a steel footing is anchored. This steel base supports the wooden conical tower. On top of the tower, a steel adapter is fitted to attach the machine housing. The nacelle includes components such as the main shaft, generator, and a yaw motor. It has a direct drivetrain without any gearbox. The wooden tower is 30 m high, including the top adapter. The rotor blades are mounted upwind of the nacelle. The carbon fiber blades are 7.5 m long, with a rotor diameter of 16 m. The wind turbine is designed for a maximum power output of 45 kW. This study leverages measurements obtained from the turbine for various operating conditions. Subsequent sections of this study will thoroughly address this test turbine's structural characteristics and operational parameters, which will be used to characterize the complete multi-body system and benchmark its properties and performance.

2.1. Tower properties

One of the novelties of this wind turbine is that the tower body is constructed using wooden modules. The body comprises five modules, each composed of four segments of laminated spruce veneer. Inside the wooden structure, 32 vertical studs of 81 × 42 mm are evenly distributed to reinforce the tower body, which has a wall thickness of 63 mm. The tower is shaped like a truncated cone where the diameter decreases with height. The outer diameter at the tower's base is 2.4 m, while the same at the top is 0.8 m. The tower is hollow and equipped with a door at the base that enables access to the inside of the tower. CAD models of the wooden tower, the steel base, and the top adapter are shown in Fig. 1. To evaluate the behaviors of the wind turbine and to characterize the structural properties of this innovative tower, a model of the tower was created using FEM. The material specifications for the wooden components are sourced from the manufacturer, and structural steel is used for the steel footing and top adapter. Given the absence of a defined modulus of elasticity for the wooden structure, the focus shifted towards quantifying the bending stiffness. This parameter is critical for characterizing the multi-body dynamics of the system. The other parts of the model were updated according to the real geometry and further refined through calibration, which was carried out using a series of tests conducted between April and May 2021, where a round collar was attached around the top of the tower and loaded with a certain force from two different directions, considering different weather conditions. This was carried out in two steps - (i) the strain gauges mounted on the tower were calibrated first and (ii) structural properties were tuned in the FE model to replicate the test data. During the pull test, the towline was first tensioned up to maximum load to allow the towline to stretch. The load was gradually released, and the sensor data were recorded accordingly to calibrate the tower model. The experimental details were documented in the B.Sc thesis [45] and hence it is omitted here.

 Table 1

 Distributed tower structural properties of the chalmers wind turbine.

Node	HtFract	TMassDen (kg/m)	TwFAStif (Nm ²)	TwSSStif (Nm ²)	Node	HtFract	TMassDen (kg/m)	TwFAStif (Nm ²)	TwSSStif (Nm ²)
1	0.000000	883.677	1.68E+10	1.68E+10	17	0.516412	244.898	1.30E+09	1.30E+09
2	0.018319	881.356	1.68E+10	1.68E+10	18	0.550095	240.816	1.18E+09	1.18E+09
3	0.044681	270.408	3.13E+09	3.13E+09	19	0.583812	235.714	1.07E+09	1.07E+09
4	0.078364	270.408	3.13E+09	3.13E+09	20	0.617494	230.612	9.64E+08	9.64E+08
5	0.112081	270.408	2.98E+09	2.98E+09	21	0.651177	225.510	8.64E+08	8.64E+08
6	0.145764	270.408	2.83E+09	2.83E+09	22	0.684894	219.388	7.70E+08	7.70E+08
7	0.179447	270.408	2.68E+09	2.68E+09	23	0.718577	213.265	6.82E+08	6.82E+08
8	0.213164	269.388	2.53E+09	2.53E+09	24	0.752260	206.122	6.00E+08	6.00E+08
9	0.246847	268.367	2.38E+09	2.38E+09	25	0.785977	200.000	5.23E+08	5.23E+08
10	0.279979	266.598	2.23E+09	2.23E+09	26	0.819660	191.837	4.53E+08	4.53E+08
11	0.314246	264.794	2.09E+09	2.09E+09	27	0.853377	184.694	3.88E+08	3.88E+08
12	0.347929	262.245	1.94E+09	1.94E+09	28	0.887060	176.531	3.29E+08	3.29E+08
13	0.38309	259.042	1.81E+09	1.81E+09	29	0.920742	168.367	2.76E+08	2.76E+08
14	0.415329	256.930	1.67E+09	1.67E+09	30	0.954460	159.184	2.29E+08	2.29E+08
15	0.449012	253.061	1.54E+09	1.54E+09	31	0.988142	150.000	1.86E+08	1.86E+08
16	0.482729	248.980	1.42E+09	1.42E+09	32	1.000000	289.855	2.51E+07	2.51E+07

After multiple iterations, the tower's distributed mass and stiffness properties were tuned to align with its first natural frequency, which equals 0.79 Hz. Additionally, deflections at different heights of the tower were also compared with the results from the test to validate the model. To replicate the actual tower, its thickness was adjusted in the model to compensate for the studs inside the tower. The resulting distributed tower properties are provided in Table 1, which contains the mass density and tower stiffness along the fore-aft (FA) and side-to-side (SS) directions corresponding to 32 nodes along the tower center line relative to its base. In this table, HtFract is the fractional height along the tower center line with respect to the base. The other key parameters reported are mass density (TMassDen) and stiffness along the fore-aft (TwFAStif) and side-to-side direction (TwSSStif), respectively. Here, it may be noted that one of the main objectives of this work is to develop the benchmark model in OpenFAST, which is widely used by researchers and engineers. Hence, the variable names mentioned above are defined following the OpenFAST convention.

The complete aero-servo-elastic model of wind turbines requires precise mode shape estimation along with the tower properties. Thus, the calibrated FE model was further used to estimate tower mode shapes. It is a cantilever made of Euler–Bernoulli beam elements representing the tower with a lumped mass at the top representing the Rotor-Nacelle Assembly (RNA), including blades. Each node has a translational and rotational degree of freedom in two orthogonal horizontal directions (i.e., X in FA and Y in SS). The first four natural frequencies are 0.79, 7.13, 22.07, and 44.12 Hz. The first two mode shapes corresponding to the fore-aft and side-to-side directions of the tower are shown in Fig. 2. The corresponding mode shape coefficients using a sixth-order polynomial as given in Eq. (1) are provided in Table 4.

$$P_i(h) = \sum_{i=2}^{6} C_{i,j} \{ f(h) \}^j$$
 (1)

In the above equation, i and h represent the mode shape number and the distance from the support, respectively.

2.2. Blade properties

The test turbine is equipped with three upwind rotor blades, each measuring 7.5 m in length, as shown in Fig. 1. These blades are made of 14 distinct airfoils at 19 nodes, each contributing to the aerodynamic profile. Detailed aerodynamic properties for specific nodes along the blade length are listed in Table 2, where the aerodynamic twist is reflected as Aero-Twist.

Numerical Manufacturing and Design Tool (NuMad) [46] is used to model the blades as flexible rotating beams attached to the hub, which vibrates in flap-wise and edge-wise directions. This modeling incorporates the actual material and geometric properties provided by

 Table 2

 Blade aerodynamics properties of the chalmers wind turbine.

	· · J · · · · · · · · · · · · · · · · ·			
Node	Nodes (m)	Aero twst (deg)	Chord (m)	Airfoil type
1	0.0000	35.0700	0.4200	Cylinder_Hono
2	0.3442	31.1884	0.4200	Cylinder_Hono
3	0.3492	31.0416	0.4200	Cylinder_Hono
4	0.6865	21.4266	0.4550	FFA-W3-357_Hono
5	0.9513	18.5855	0.5104	FFA-W3-360_Hono
6	0.9864	18.2095	0.5177	FFA-W3-330_Hono
7	1.0376	17.6356	0.5272	FFA-W3-301_Hono
8	1.1987	15.7822	0.5488	FFA-W3-270_Hono
9	1.3494	14.0359	0.5691	FFA-W3-240_Hono
10	1.6596	10.0248	0.5791	FFA-W3-211_Hono
11	2.6155	2.1538	0.5021	NACA-63-218_Hono
12	4.4462	-1.9223	0.3477	NACA-63-215_Hono
13	5.3526	-0.2875	0.2713	NACA-63-214_Hono
14	6.4009	-0.7119	0.1829	NACA-63-213_Hono
15	7.0450	-0.9994	0.1286	NACA-63-238_Hono
16	7.3846	0.2858	0.1000	NACA-63-212_Hono
17	7.4382	2.0945	0.0850	NACA-63-212_Hono
18	7.4727	3.2192	0.0600	NACA-63-212_Hono
19	7.4880	3.6568	0.0400	NACA-63-212_Hono

 Table 3

 Distributed blade structural properties of the chalmers wind turbine.

BlFract	AeroCent	Aero	BMassDen	FlpStff (Nm ²)	EdgStff (Nm ²)
		twst(deg)	(kg/m)		
0.00000	0.25	35.0700	39.50	1.842E+07	1.824E+07
0.04462	0.25	31.4700	39.50	1.842E+07	1.223E+07
0.08937	0.25	21.6000	17.80	6.821E+06	1.221E+07
0.13412	0.25	18.0000	16.30	4.270E+06	1.057E+07
0.17874	0.25	14.1500	14.40	2.626E+06	8.871E+06
0.22350	0.25	9.8100	12.60	1.716E+06	6.820E+06
0.26825	0.25	7.0100	10.40	1.033E+06	4.572E+06
0.31287	0.25	3.3800	8.45	0.583E+06	2.922E+06
0.35762	0.25	1.8500	7.15	0.357E+06	2.127E+06
0.40237	0.25	0.8900	6.02	0.211E+06	1.640E+06
0.44699	0.25	0.2100	5.01	0.131E+06	1.166E+06
0.49174	0.25	-0.4500	4.15	0.0767E+06	0.847E+06
0.53649	0.25	-1.1200	3.66	0.0511E+06	0.643E+06
0.58111	0.25	-1.7600	3.34	0.0411E+06	0.517E+06
0.62587	0.25	-2.3800	3.00	0.0286E+06	0.401E+06
0.67062	0.25	-1.6000	2.70	0.0201E+06	0.317E+06
0.71524	0.25	-0.2400	2.50	0.0168E+06	0.242E+06
0.75999	0.25	-0.4200	2.29	0.0123E+06	0.187E+06
0.80474	0.25	-0.5400	2.04	0.0095E+06	0.132E+06
0.84936	0.25	-0.7000	1.79	0.0074E+06	0.084E+06
0.89411	0.25	-0.8300	1.54	0.0041E+06	0.052E+06
0.93887	0.25	-1.0100	1.29	0.0032E+06	0.031E+06
0.98348	0.25	0.0000	1.04	0.0021E+06	0.017E+06
0.99534	0.25	3.0000	0.66	0.0004E+06	0.005E+06
1.00000	0.25	4.0000	0.52	0.0002E+06	0.003E+06

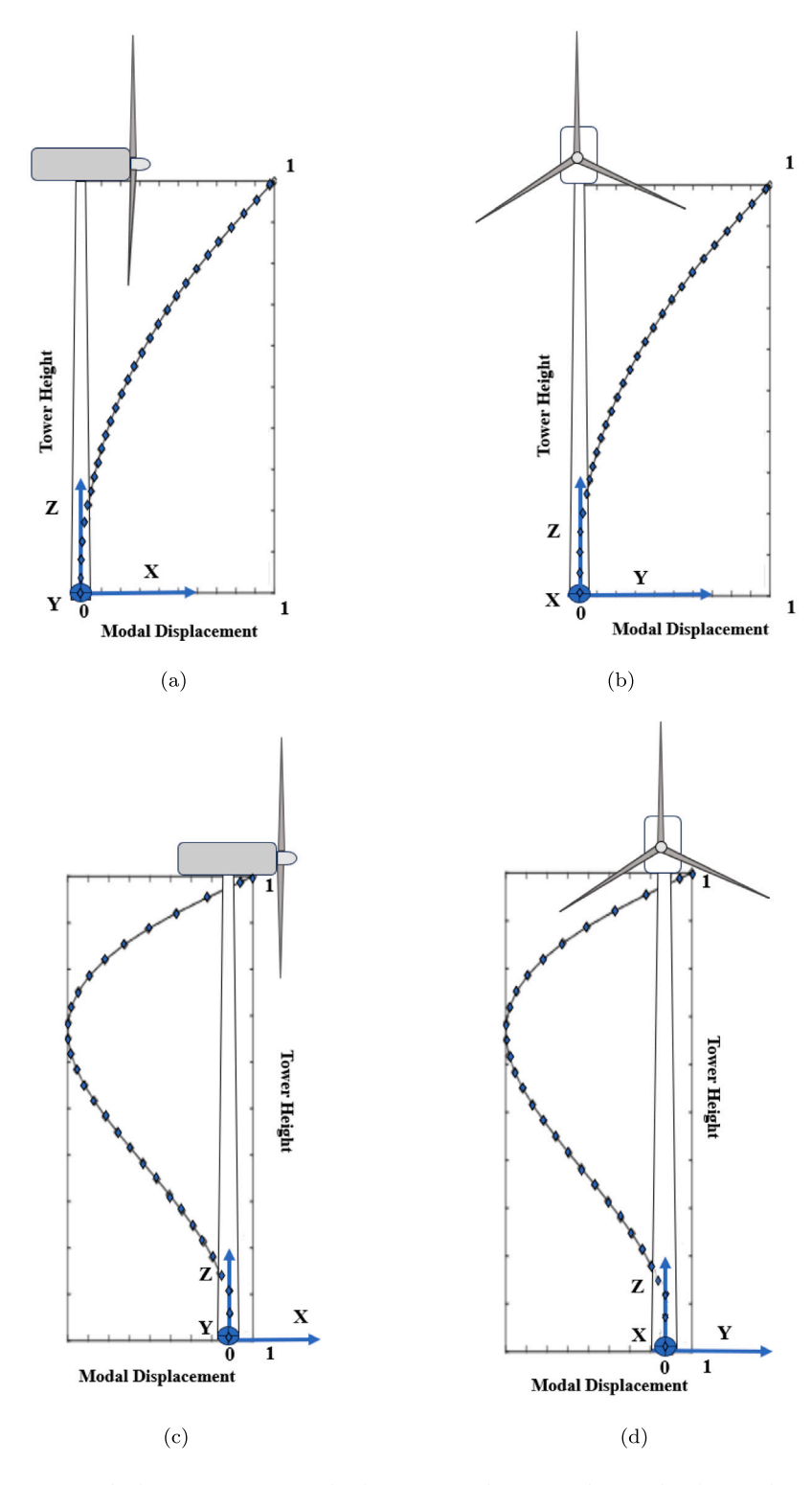


Fig. 2. Tower mode shapes; (a) First FA Mode, (b) First SS Mode,(c) Second FA Mode, (d) Second SS Mode.

the manufacturer and the aerodynamic properties listed in Table 2. Fig. 3 shows the blade model in the NuMad graphical user interface and the airfoils' shape. This paper does not include comprehensive details on the airfoil characteristics, as it mainly focuses on wind and power calibration. The authors will provide these blade details in the subsequent work, where the major emphasis will be on blade response characterization. The NuMAD model is then exported to ANSYS [47] for further finite element simulation. The boundary conditions applied to the blade resemble those of a cantilever beam, with the blade being

fixed at the root and free at the tip. The optimal mesh was selected based on the standard mesh test for the modal analysis to obtain higher accuracy. The first four natural frequencies of the blade in Hz are 5.63, 13.82, 18.96, and 32.97, representing 1st flapwise, 1st edgewise, 2nd flapwise, and 1st torsional frequencies, respectively. These frequencies will be verified through inverse identification of modal properties in the subsequent section of this paper. The respective blade mode shapes are shown in Fig. 4, and the mode shape coefficients for the first three modes are provided in Table 4. In this table, r represents the distance

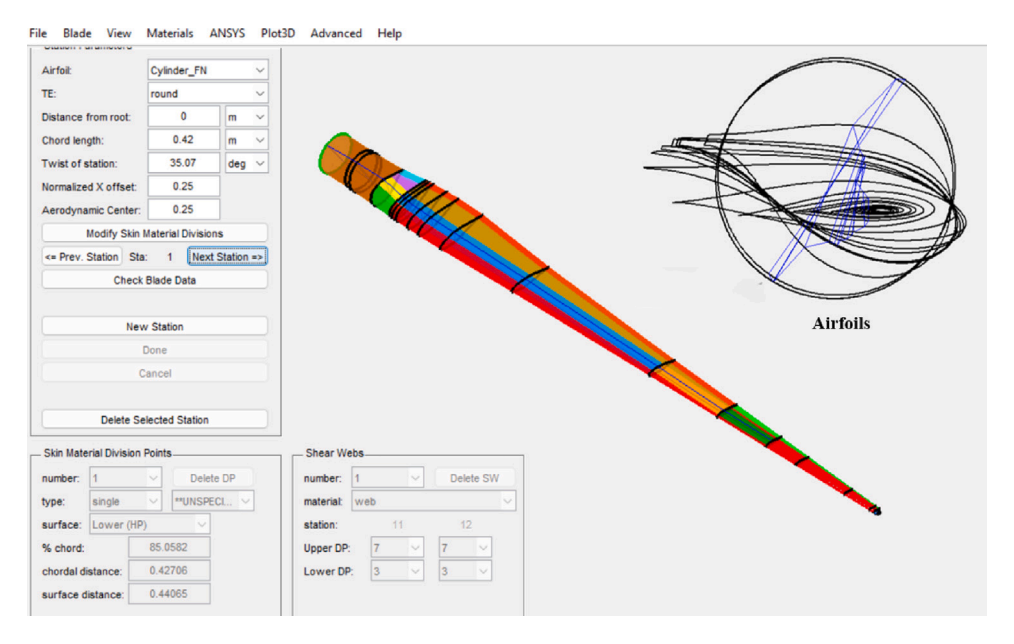


Fig. 3. Blade model of Chalmers wind turbine as viewed in the NuMAD GUI with airfoils.

of a point on the blade's longitudinal axis from its root, while R and R_H represent the radius of the blade and hub, respectively.

Besides modal characteristics, the distributed structural properties of the blades are also evaluated from PreComp [48] using the NuMAD model, which is listed in Table 3. The fractional separation between the chord line and the pitch axis is represented by the term AeroCent. The structural twist of the blade, i.e., StrcTws is assumed to be identical to the aerodynamic twist as given in Table 2, and BMassDen represents the mass per unit length. The flap-wise and edgewise stiffness properties are marked as FlpStff and EdgStff, respectively in this table.

2.3. Hub, nacelle, and drive train properties

This section presents the hub, nacelle, and drivetrain properties of the test turbine. As discussed earlier, the tower body is made up of wooden modules. The height of the tower above ground level is 29.095 m. On top of the tower, a steel top adapter is fitted to attach the rotor-nacelle assembly. In its undeflected configuration, the hub of the test turbine is located at a height of 29.393 m above ground level, having a mass of 2799 kg. The vertical distance from the tower top to the rotor shaft is 0.292 m, and the distance from the yaw axis to the rotor apex is 0.608 m. The distance from the rotor apex to the blade root and tip are 0.45 m and 7.95 m, respectively, with no PreCone angle. The nacelle has a mass of 6500 kg, with the center of mass (i.e., CM) located at 0.563 m downwind of the yaw axis and 0.906 m above the yaw bearing. The nacelle inertia about the yaw axis is taken to be 6500 kg-m², while the hub inertia about the rotor axis is taken as 255 kg-m². The test turbine has a high-speed direct drive train. The generator's electrical efficiency is kept at 99.9% with a gearbox ratio of 1 (i.e., this value is assumed for FAST modeling replicating no gearbox in the drivetrain). The generator inertia about the high-speed shaft is taken to be 137 kg-m2, equivalent driveshaft linear-spring and damping constants are 7.72E+06N-m/rad and 5.4E+04N-m/(rad/s), respectively.

3. Generator-torque and blade-pitch controller details

This section discusses the baseline torque and pitch control system used in the test turbine, along with different parameters selected for the simulation in OpenFAST. First, the generator torque control is discussed, followed by the pitch controller details used in this study.

Table 4Mode Shape Coefficients of Tower and Blade.

j	Tower			Blade			
	$\{f(h)\}^j$	$(C_{1,j})$	$(C_{2,j})$	$\{f(r)\}^j$	$(C_{1,j})$	$(C_{2,j})$	$(C_{3,j})$
2	$(h/H)^2$	0.37629	-25.07030	$\left[\frac{r}{(R-R_H)}\right]^2$	0.0325	0.0005	-0.0881
3	$(h/H)^3$	2.30263	-41.35770	$\left[\frac{r}{(R-R_H)}\right]^3$	-0.0798	4.3158	3.5029
4	$(h/H)^4$	-4.19699	84.88334	$\left[\frac{r}{(R-R_H)}\right]^4$	1.7036	-7.7918	-25.3911
5	$(h/H)^5$	3.94659	09.43586	$\left[\frac{r}{(R-R_H)}\right]^5$	-0.0235	6.8929	37.2812
6	$(h/H)^6$	-1.42852	-26.89120	$\left[\frac{r}{(R-R_H)}\right]^6$	-0.6327	-2.4174	-14.3049

There are five control zones where the generator torque is regulated depending upon the flow conditions, as shown in Fig. 5. Generator torque is zero in Region 1 before cut-in wind speed, where no power is extracted from the wind; instead, the wind accelerates the rotor for start-up. Region 2 (i.e., cut-in to rated condition)is a control region for optimizing power. In this region, the generator torque is proportional to the square of the filtered generator speed to maintain a constant (i.e., optimal) tip-speed ratio. Region 11/2 is a linear transition zone between Region 1 to Region 2. This region places a lower limit on the generator speed to cap the wind turbine's operational speed range. Another linear transition zone between Regions 2 and 3 (i.e., Region 21/2) is typically needed to limit tip speed at rated power. Finally, the generator power is retained constant in Region 3 (i.e., rated to cut-out condition) so that the generator torque is inversely proportional to the filtered generator speed. The peak power coefficient of 0.42 occurred at a tip-speed ratio of 9.87. Given a gearbox ratio of 1:1, this corresponds to an optimal constant of proportionality of 35.17 Nm/(rad/s²) in the Region 2 control law for optimal generator torque as per [49].

Once the operating parameters for the generator are established for two different power outputs, 25 kW and 30 kW, respectively. The rated generator speed is uniformly set at 7.45 rad/s, corresponding to a power of 25 kW with a generator efficiency of 99.9% for a mechanical power of 25.025 kW at a generator torque of 3359.06N-m. On the other hand, the 30 kW setting resulted in a generator torque of 4030.88N-m. The transition speeds from one region to another (i.e., Region 1 to Region 1½, Region 1½ to Region 2, and Region 2½ to Region 3) are taken as 5.7 rad/s, 6.2 rad/s, and 7.0 rad/s, for 25 kW configuration and 5.7 rad/s, 6.2 rad/s, and 7.2 rad/s for 30 kW configuration,

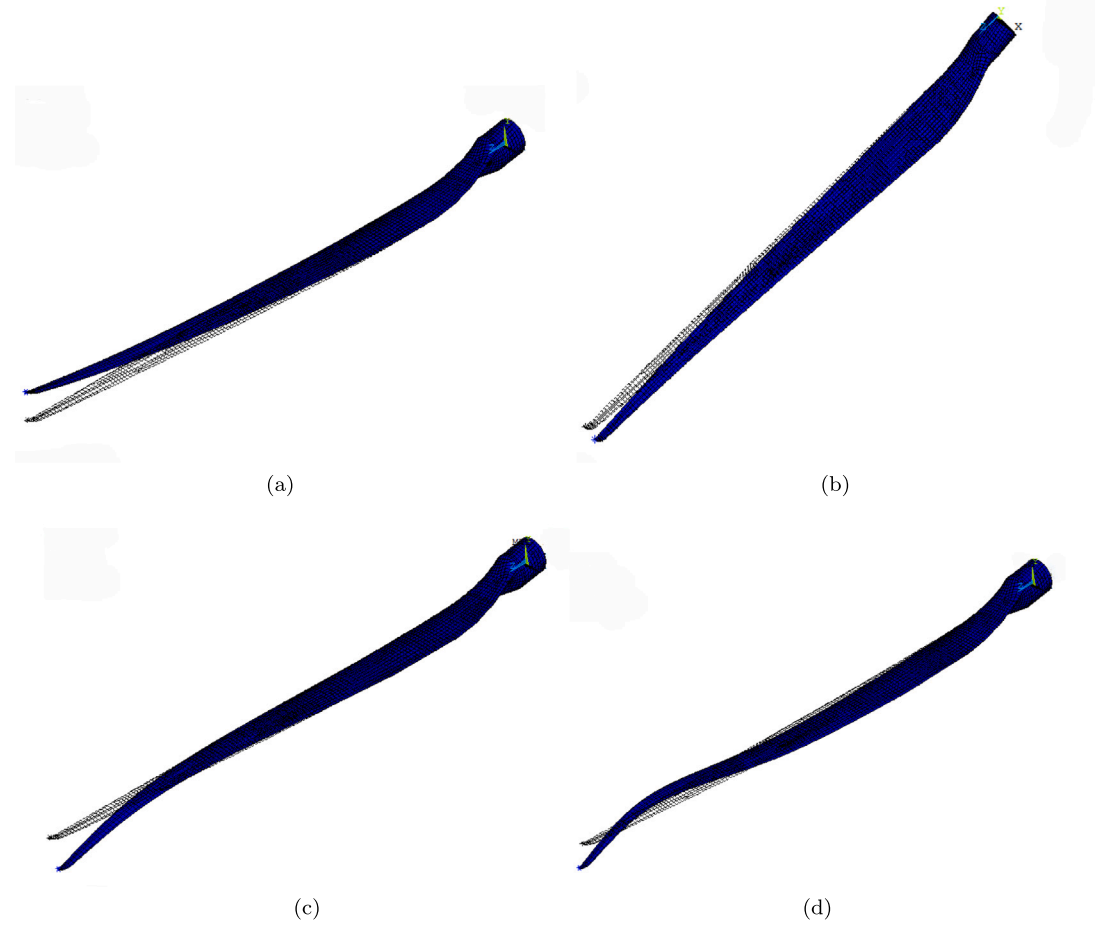


Fig. 4. Blade model and identified mode shapes; (a) First Flapwise, (b) First Edgewise, (c) Second Flapwise (d) First Torsional.

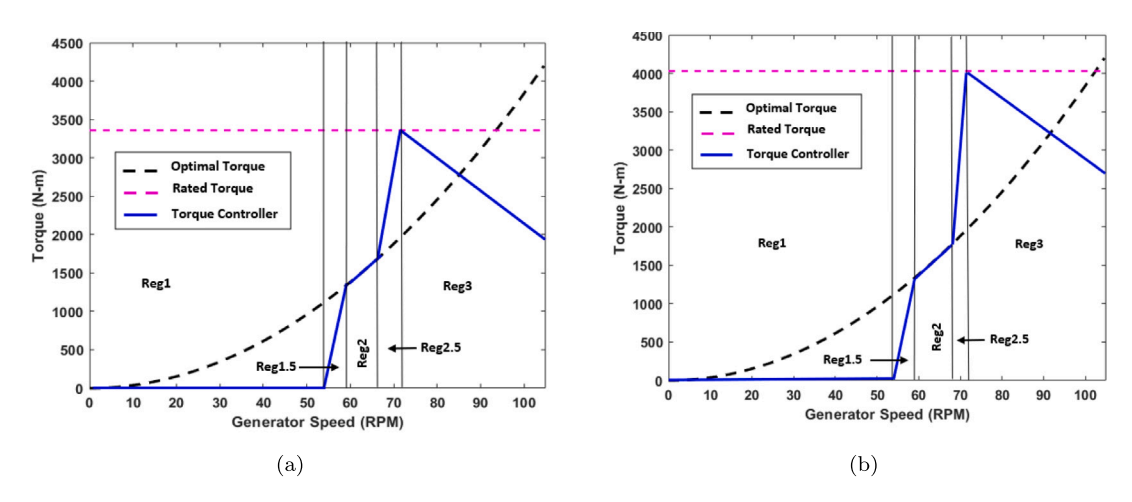


Fig. 5. Generator torque and speed in different control regions; (a) for 25 kW power setting, (b) for 30 kW power setting.

respectively. A consistent generator-slip percentage of 10% is adopted in Region $2^1/2$ for both configurations, similar to the value used in the DOWEC study [51]. To safeguard against potential overloads, the torque is capped at a maximum of 4500.00 N-m, and a torque rate limit of 10,000 N-m/s is enforced. The generator-torque versus generator speed response curve of the test turbine for the two power settings are illustrated in Fig. 5(a) and Fig. 5(b), respectively.

In Region 3, the blade-pitch control system takes over to maintain the generator speed above the rated flow. A full-span blade pitch controller used in this study is a single-variable device that changes the blade pitch angle to reduce generator speed fluctuation. The full-span rotor-collective blade-pitch-angle commands are computed using gain-scheduled proportional-integral (PI) control on the error between the filtered and rated generator speeds. The reference generator speed is established at 7.85 rad/s for activating the pitch controller. The system allows for a range of pitch angles from a minimum of 0.034 rad to a maximum of 1.5707 rad, with the maximum pitch rate limited to 0.2 rad/s to ensure smooth transitions. Following the procedure explained for the NREL 5 MW benchmark turbine [52], the pitch controller's proportional (K_P) and integral (K_I) gains at the minimum pitch angle

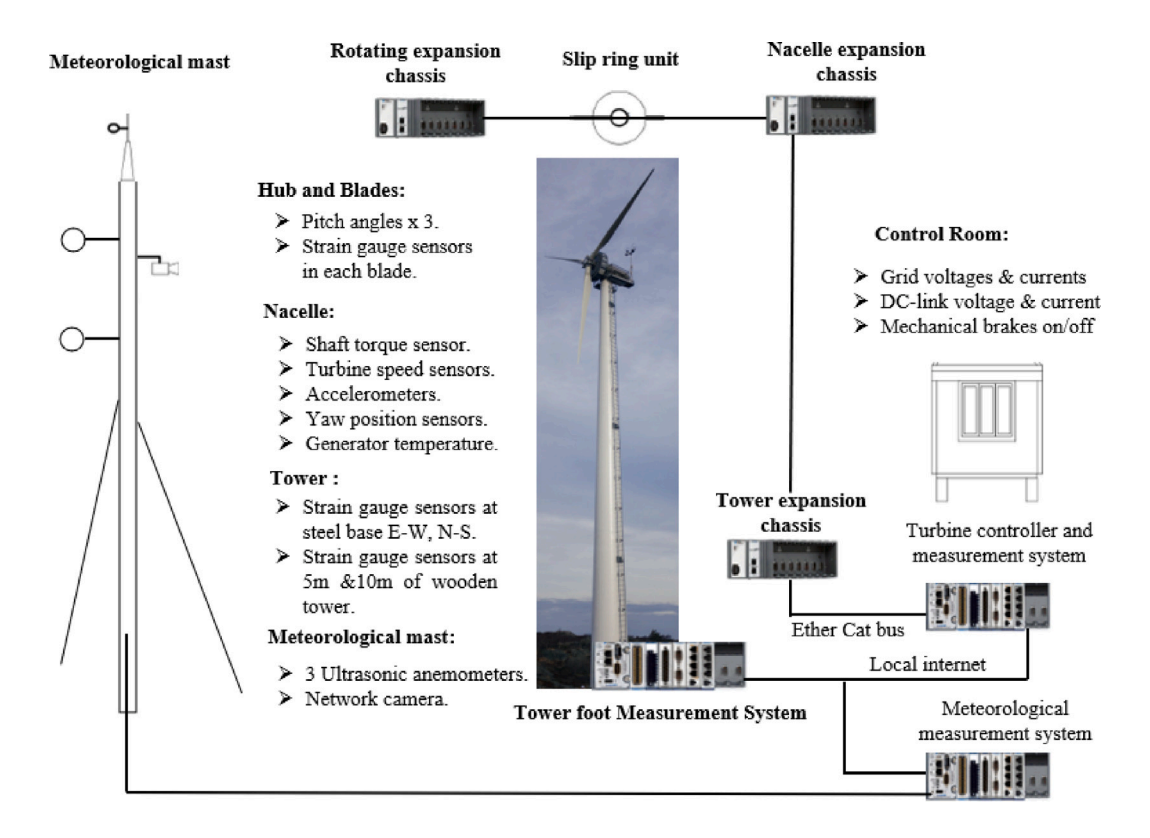


Fig. 6. Layout of the measurement and control system of Chalmers wind turbine [50].

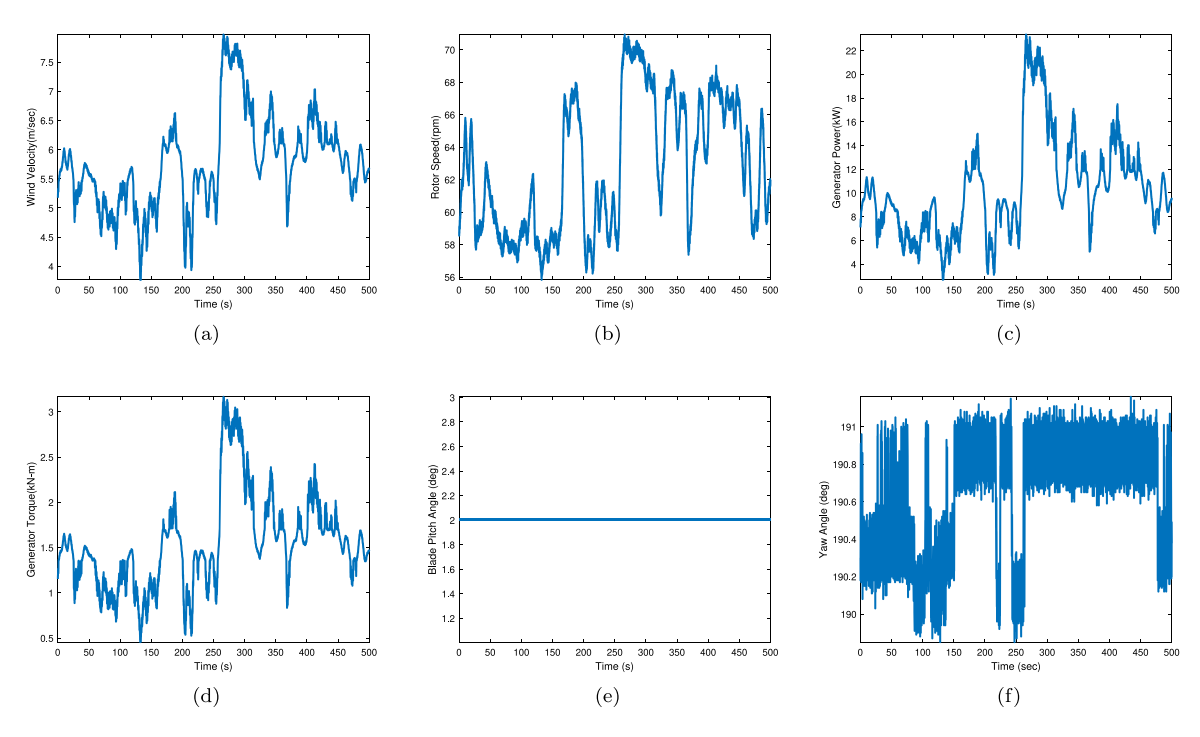


Fig. 7. Operating Conditions of Chalmers Wind Turbine with average wind 5.9 m/s; (a) Wind Velocity at hub height, (b) Rotor Speed, (c) Generator Power (d) Generator Torque, (e) Blade Pitch angle, (f) Yaw Position.

are set to 0.35 s and 0.22, respectively. Additionally, the blade-pitch angle at which the pitch sensitivity has doubled from its value at the rated operating point (θ_k) is determined as 0.4 rad, corresponding to the point where the derivative gain (K_D) is zero. This meticulous setup

ensures that pitch adjustments are responsive and tempered, enhancing the turbine's efficiency while safeguarding the mechanical integrity of the system. The baseline control system parameters are supplied to the test turbine through the controller input panel built on LabVIEW [53]

Table 5
Measurement channel details of chalmers wind turbine.

Location	Channel details	No of channels	Location	Channel details	No of channels
Hub and	Strain gauges @ blades	15		Strain gauges @ Foundation	2
blade	Pitch angles	3	Foundation and Tower	Stain gauges @ steel base	5
Diade	Pitch position	3		Strain gauges @ wooden tower	8
	Shaft torque	2		FFR regulator	2
	Rotor speed	2	Control room	Generator	3
Nacelle	Accelerometers	3	Control room	DC-link current	1
Nacelle	Generator temperature	4		Grid Frequency an Power waste	2
	Yaw position	2	Met Mast	Anemometers	6
	Air pressure, temperature, humidity	3	wet wast	Network camera	1

interface for the measurement record and to the OpenFAST model as an external dynamic link library (DLL) [54] for the simulations.

4. Sensor configuration & field measurements

The test turbine has several sensors, including strain gauges on different structural components. The turbine's measurement and control system layout is shown in Fig. 6. This system is centered around the Compact Rio hardware [55] from National Instruments, interfacing with an expansion chassis in the nacelle and tower via an EtherCat bus. Programming for the system is developed in LabVIEW [53]. The control and measurement system operates with dual sampling frequencies of 100 Hz and 20 Hz for signal measurements, capturing data from 67 channels summarized in Table 5. The collection of data for a longer time duration is available at the Zenodo repository [56,57]. Details on the complete measurement setup and sensor configurations are documented in the bachelor's thesis [58]. Notably, the wind estimation derived from Eq. (5) outlined in Section 5.2 serves as a basis for comparison with the EKF-estimated wind, considered the recorded wind in the subsequent sections of this paper.

Figs. 7 to 9 show the data recorded from different sensors at 20 Hz under three operating conditions. Out of these three plots, the first one, i.e., Fig. 7, shows the response of the turbine recorded on 23rd September 2022 at a mean wind speed of 5.9 m/s at hub height corresponding to the below-rated condition. The critical parameters shown here are rotor speed, generator power, and generator torque when the blade pitch controller remained inactive as the wind speed did not exceed the threshold for pitch control activation. Besides the belowrated condition, Fig. 8 demonstrates the above-mentioned responses, recorded on 17th January 2022 at a mean wind speed of 9.2 m/s. Notably, the torque control parameters, as detailed in Section 3, for the 25 kW power setting, are employed for this case. Fig. 9 represents the operating condition of the test turbine recorded on 5th January 2023, employing the control settings tailored for the maximum power output of 30 kW. Measurements spanning a total duration of 500 s are shown in Fig. 9. During this interval, the average wind speed was around 7.9 m/s, originating from the southwest. The rotor speed maintained a range from ~ 60 rpm to 78 rpm, while the blade pitch was adjusted between 4 and 11 degrees to sustain the target power output of 30 kW, as demonstrated in Figs. 9(a) to 9(f).

As mentioned earlier, there are 67 channels, including multiple strain gauges in the tower and blade. In the transition between the wooden structure and the concrete foundation is the steel footing, where a total of eight strain gauges have been placed as two sensors. Refer to Fig. 10 for the details of these sensor placements. These are positioned in the north-south and east–west direction at a height of 0.53 m, representing one-third of the height of the steel footing. Each blade consists of 8 strain gauges placed along the length of the blade, positioned at the blade root, at a distance of 2 m, 3.5 m, and 5 m away from the blade root.

Table 6
Identified tower and blade frequencies from tower and blade root measurements.

Record date	Mean wind (m/s)	Actual and identified frequencies (Hz)						
		Tower		Blade				
		1st freq.	Identified	1st Flap freq.	Identified			
29-01-2022	21.9		0.82 [3.79]		5.42 [3.73]			
17-01-2022	9.22	0.79	0.82 [3.79]	5.63	5.41 [3.90]			
05-01-2023	7.92	0.79	0.82 [3.79]	5.05	5.41 [3.90]			
23-09-2022	5.93		0.82 [3.79]		5.40 [4.08]			

N.B.: The values within [.] indicate the percentage error between the actual and identified frequencies.

5. Inverse analysis using field measurements

This section uses measured response quantities to identify in-situ structural parameters, which are further needed for model validation. This is carried out in two steps. First, the modal parameters are extracted through signal processing, where any time–frequency analysis (e.g., short-time Fourier transform [59], Hilbert-Huang transformation [60], wavelet transformation [61], among many others) can be adopted. In this study, the continuous wavelet transform is used for signal processing. The rationale behind the selection of wavelet-based time–frequency analysis is due to its superior ability in signal processing, which has already been established in the literature [62,63]. Once the modal parameters are identified, the rotor effective wind speed is estimated to tune the simulated turbine responses with field measurements.

5.1. Modal identification of tower and blade from measurements

As stated earlier, the Wavelet Transform (WT) has an inherent advantage compared to other time–frequency representation techniques when extracting instantaneous features from signals. In wavelet analysis, a signal f(t), a function of time, is expressed with a composition of several time-localized, translated, and scaled basis functions, $\psi_{a,\tau}(t)$, called the mother wavelet. The Continuous Wavelet Transform (CWT) processes a time signal f(t) and converts it into a new 2D sequence. This transformation yields the wavelet coefficients $W_f(a,\tau)$ and is mathematically defined as follows [64]

$$W_f(a,\tau) = \frac{1}{\sqrt{a}} \int_{-\infty}^{+\infty} f(t) \, \psi^* \left(\frac{t-\tau}{a} \right) dt \; \; ; \; \; a,\tau \in R \tag{2}$$

The shift parameter τ is used to center the wavelet function to obtain information about the signal around the location $t=\tau$. The scale parameter a, which is inversely proportional to frequency, can be varied to extend the basis function to control the range of frequencies about which information can be obtained, and $\psi_{a,\tau}^*(.)$ is the complex conjugates of the mother wavelet $\psi_{a,\tau}(.)$. For a discrete-time series

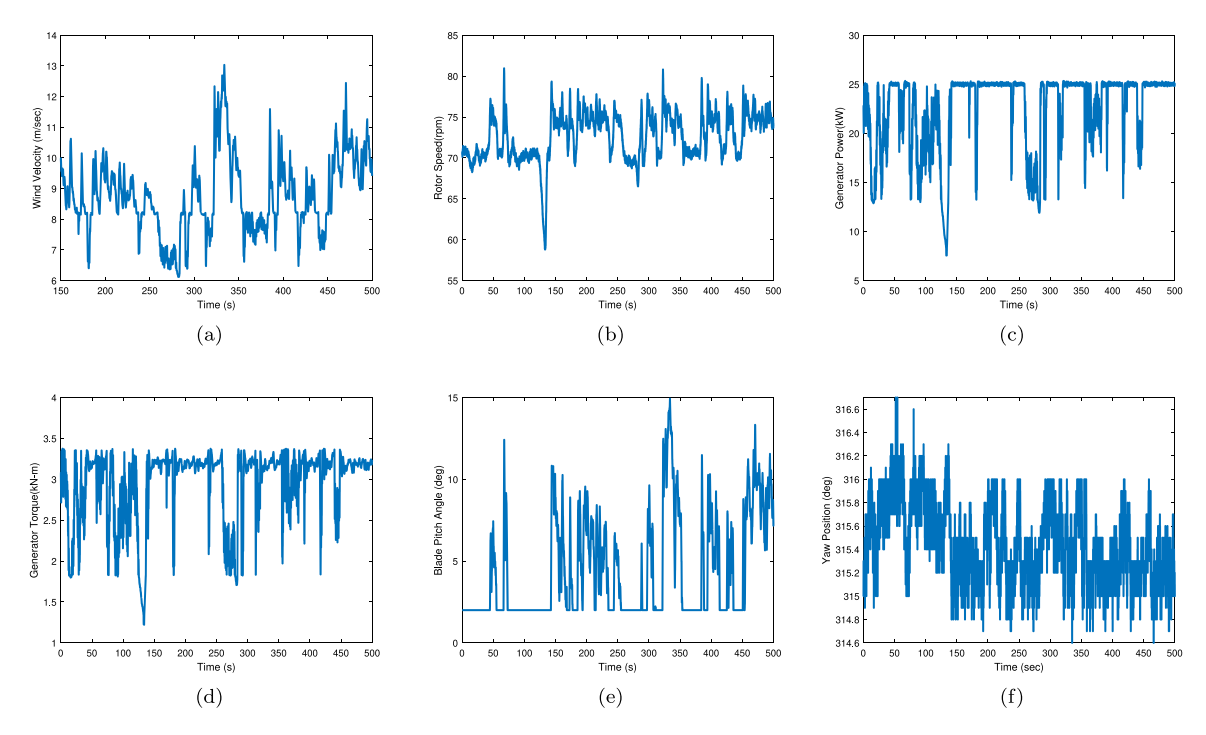


Fig. 8. Operating Conditions of Chalmers Wind Turbine for rated conditions with average wind 9.2 m/s; (a) Wind Velocity at hub height, (b) Rotor Speed, (c) Generator Power, (d) Generator Torque, (e) Blade Pitch angle, (f) Yaw Position.

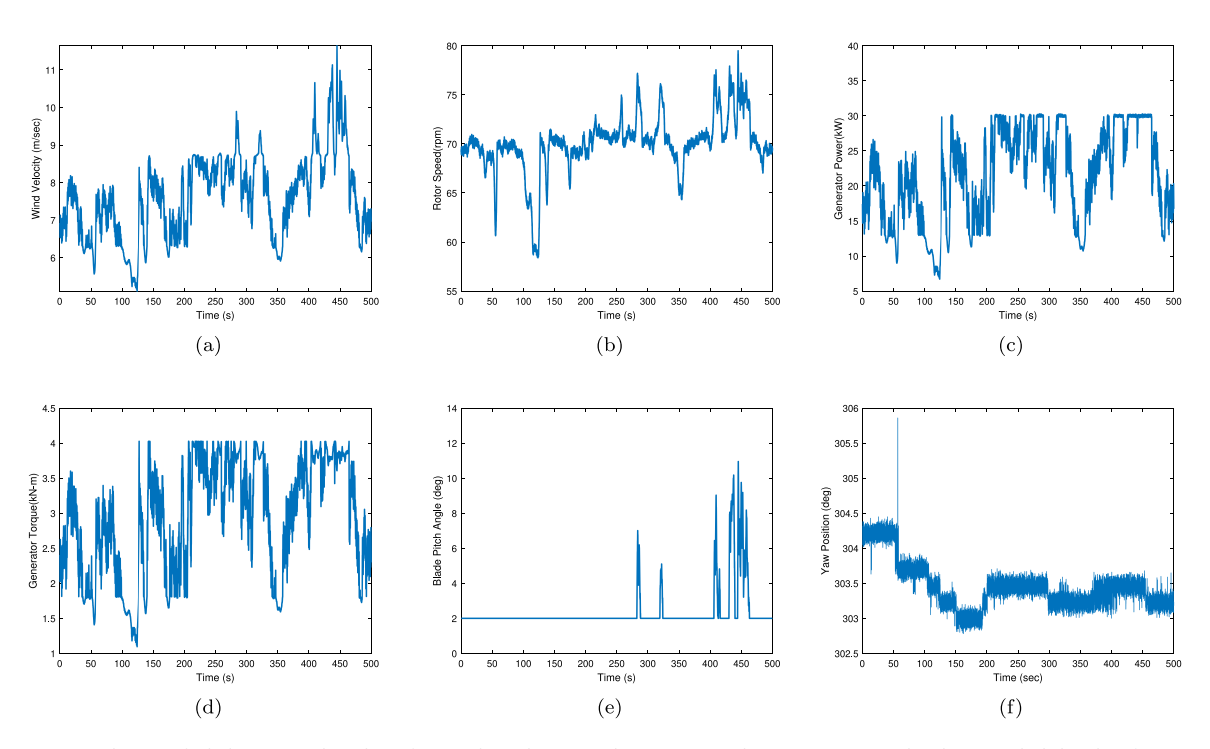


Fig. 9. Operating Conditions of Chalmers Wind Turbine for rated conditions with average wind 7.9 m/s; (a) Wind Velocity at hub height, (b) Rotor Speed, (c) Generator Power (d) Generator Torque, (e) Blade Pitch angle, (f) Yaw Position.

signal, $y_n(t)$ having N data points and dt time step, can be expressed in the frequency domain using CWT as

$$W_{\psi} \, \tilde{y}_{k}(a,n) = \sum_{k=0}^{N-1} \tilde{y}_{k} \, \tilde{\psi}^{*}(a \, \omega_{k}) e^{i \, \omega_{k} \, n \, dt}$$
 (3)

 \tilde{y}_k and $\tilde{\psi}^*$ are the discrete Fourier transform of the signal and the mother wavelet, respectively. In essence, the continuous wavelet transform convolves the mother wavelet $\psi_{\tau,s}$ with the signal f(t). The wavelet coefficients take on maximum values at the locations where the

frequency of the scaled wavelet f_0 coincides with the local frequency of the signal $f_i(t)$. This defines the ridges in the time–frequency plane as $a_r(\tau) = \frac{2\pi f_0}{f_i(t)}$. Extracting the values of the wavelet coefficients along each ridge yields a wavelet skeleton. Similarly, a slice of the scalogram at a given time, across the range of frequencies, yields the instantaneous spectrum of the signal, indicating the frequency content at that instant in time. By finding out the points where wavelet coefficients reach local maxima i.e., $\left|W_f(a_r,\tau)\right| = \left(\left|W_f(a,\tau)\right|\right)_{\max}$, the corresponding frequencies can be identified.

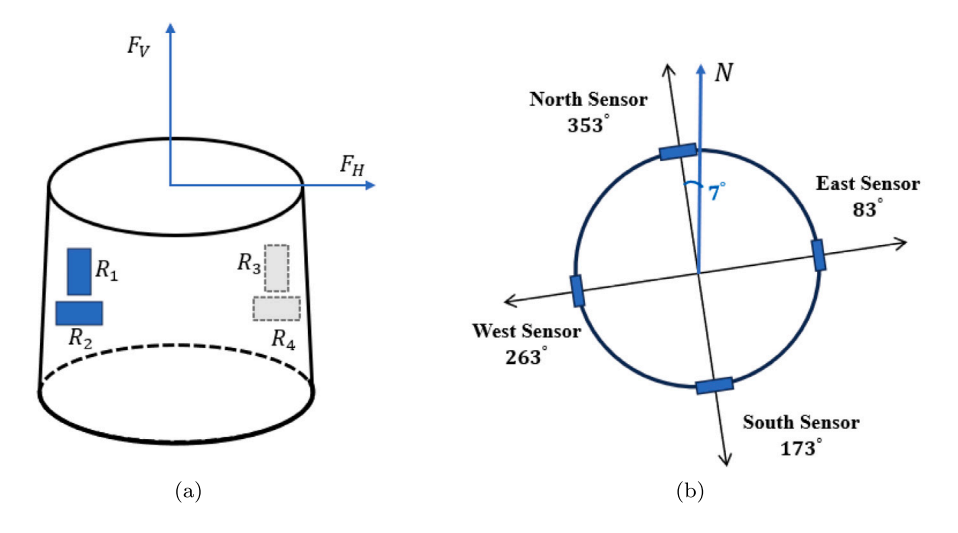


Fig. 10. Sensors in the Steel Base; (a) Orientation of the strain gauges, (b) Compass Directions.

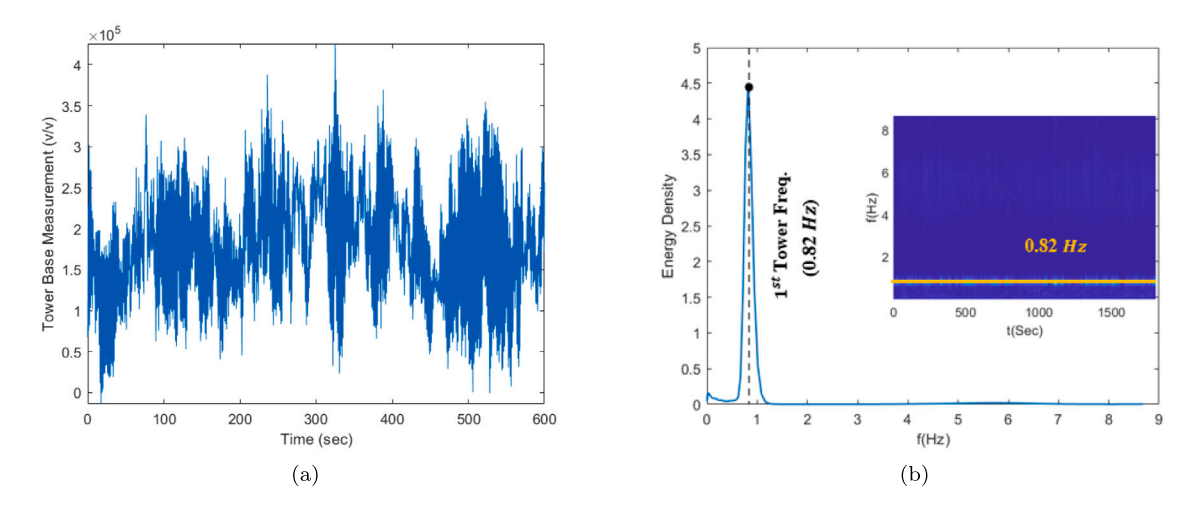


Fig. 11. Wooden tower response in parked condition (i.e., mean wind speed of 21.9 m/s); (a) Base moment along the fore-aft direction, (b) Energy spectrum with wavelet scalogram in inset.

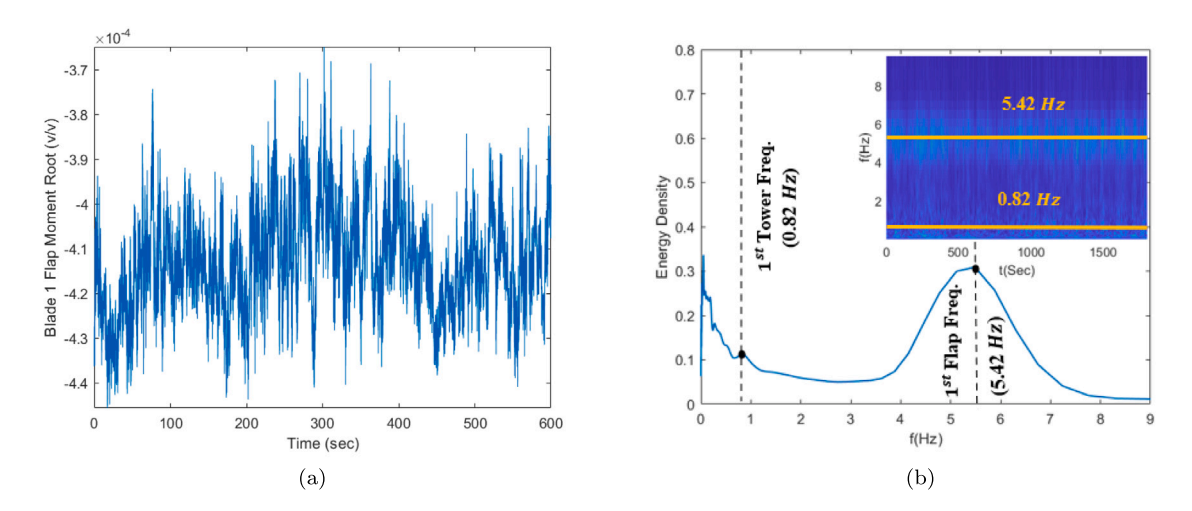
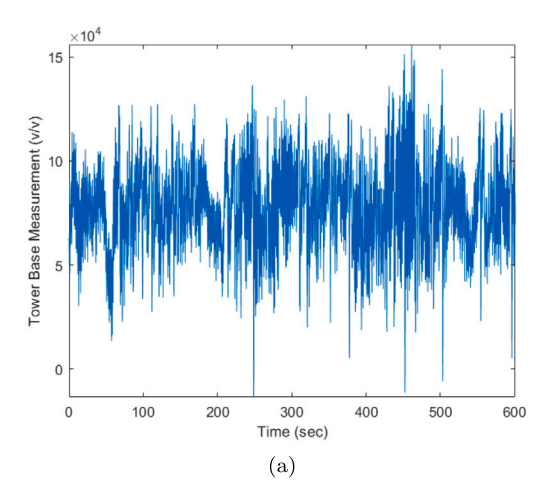


Fig. 12. Blade response in parked condition (i.e., mean wind speed of 21.9 m/s); (a) Root moment along flap wise direction, (b) Energy spectrum with wavelet scalogram in inset.



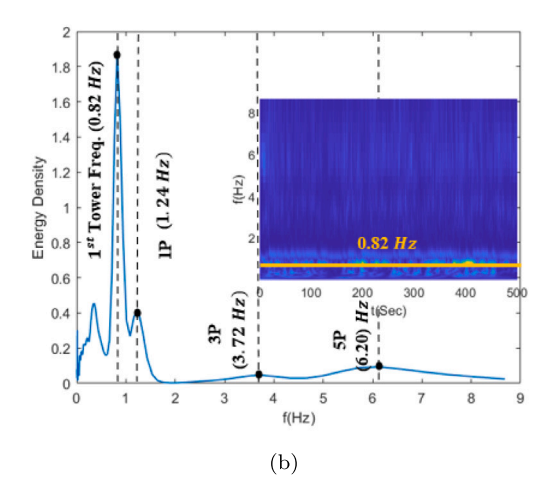


Fig. 13. Tower base measurement and corresponding CWT scalogram with the energy density for operating condition with mean wind 9.2 m/s; (a) Tower base measurements along fore-aft direction, (b) Identified tower frequencies.

Table 7RRMSE and TRAC values of simulated and measured responses.

Responses	Responses Wind speed (m/s)		Rotor speed	Rotor speed (rpm)		Generator torque (kN-m)		Generator power (kW)	
Record date	RRMSE	TRAC	RRMSE	TRAC	RRMSE	TRAC	RRMSE	TRAC	
23-09-2022	0.027	0.999	0.004	0.999	0.033	0.998	0.034	0.998	
05-01-2023	0.031	0.999	0.008	0.999	0.061	0.996	0.062	0.996	
17-01-2022	0.049	0.997	0.009	0.999	0.104	0.990	0.102	0.991	

In this context, it may be noted that the resolution of the scalogram sometimes needs to be enhanced using different advanced versions of the CWT, e.g., Combined Wavelet Hilbert Transformation [65] or Synchro-squeezing [66]. These are particularly required when there are closely spaced modes or poor resolution of the energy spectrum, leading to erroneous frequency tracking. However, as the frequencies of the HAWT used in this study are well separated and the resolution of the spectrogram did not offer any difficulty in frequency tracking, these advanced versions were not invoked, and a regular CWT was found to be sufficient to meet the objectives. Thus, an analytic Morse wavelet, a complex-valued wavelet containing positive real-frequency components, is employed for the modal identification. This choice of wavelet offers the inherent advantage of effectively representing signals with varying amplitudes and frequency content over time [67,68] and free from the end effect errors arising from time resolution [20]. The amplitude spectrum of this wavelet in the frequency domain is given by

$$\psi_{\alpha,\gamma}(\omega) = H(\omega) a_{\alpha,\gamma} \omega^{\alpha} e^{-\omega^{\gamma}}$$
(4)

In this equation, $H(\omega)$ is the Heaviside step function, and $a_{\alpha,\gamma}$ represents a normalizing constant. These parameters are crucial and signify the compactness and symmetry of the wavelet. The time-bandwidth product of the resulting wavelet, characterizing the trade-off between time and frequency localization, is determined as $P^2 = \alpha \times \gamma$. Efficient algorithms for computing Morse wavelet coefficients, developed by Lily [69], are available in MATLAB [70], which is utilized in this study. The Morse wavelet exhibits zero skewness when the symmetry parameter γ is set to 3. Hence, for this study, default parameter values of $\gamma = 3$ and a specific value for α corresponding to the time-bandwidth product value as 60 are employed to ensure symmetry in the basis function.

To identify the tower frequencies, the measurements of tower root moments with a sampling frequency of 20 Hz are considered. Here, it may be noted that turbine response during regular operating conditions has contributions from both structural and rotational frequencies of the turbine. Therefore, to avoid false identification of structural frequencies, the parked condition is chosen first. Fig. 11 and Fig. 12 show the

recorded measurements of the tower and blade during this condition. These measurements were recorded on 29th January 2022 at a mean wind speed of 21.9 m/s. The energy spectrum shows the identified tower and blade frequencies along the fore-aft and flapwise directions, which are 0.82 Hz and 5.42 Hz, respectively. The estimated error for these frequencies is well within 5% with respect to the designed frequencies for the respective structural components. Similarly, the tower and blade measurements in orthogonal directions (i.e., side-to-side and edge-wise, respectively) are also considered to identify the respective structural frequencies, which are not presented here to avoid repetition. Once these frequencies are identified, this process is repeated for other operating conditions to cross-verify these results. Thus, Fig. 13 shows the tower base measurement and the corresponding CWT scalogram with the instantaneous spectra demonstrating the energy density across ridge frequencies obtained from the wavelet analysis, respectively, at an average wind speed of 9.2 m/s. As stated earlier, the energy density across ridge frequencies shows the tower 1st fore-aft frequency at 0.82 Hz with 3.79 % error as compared to the frequency obtained from the FEM model. This plot also shows the presence of other frequencies in the spectrum, as expected, which can be easily identified further. Simultaneously, the blade frequencies were verified, analyzing blade root measurements in the flapwise directions. Fig. 14 shows similar results for the blades corresponding to a mean wind speed of 9.2 m/s. The first flapwise frequency identified from this measurement displays 3.90% estimation error compared to the NuMAD model. Besides structural frequencies, rotational frequencies of the turbine and its harmonics are also identified from the response during regular operating conditions, which are marked in the respective plots. Table 6 enumerates the identified frequencies and their comparison with the frequencies estimated from the FEM models of the tower and blade, which establishes the accuracy of the inverse system characterization.

5.2. Wind field characterization

The rotor effective wind speed has been derived using two different methods in this paper. In the first method, the rotor effective wind

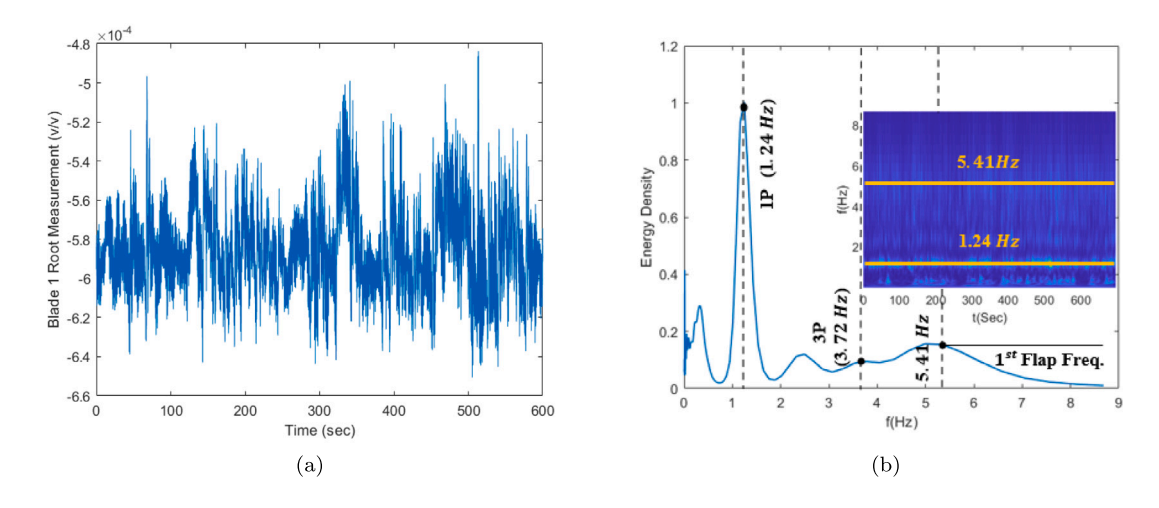


Fig. 14. Blade root measurement and corresponding CWT scalogram with the energy density for operating condition with mean wind 9.2 m/s; (a) Root measurement along flap wise direction, (b) Identified blade frequencies.

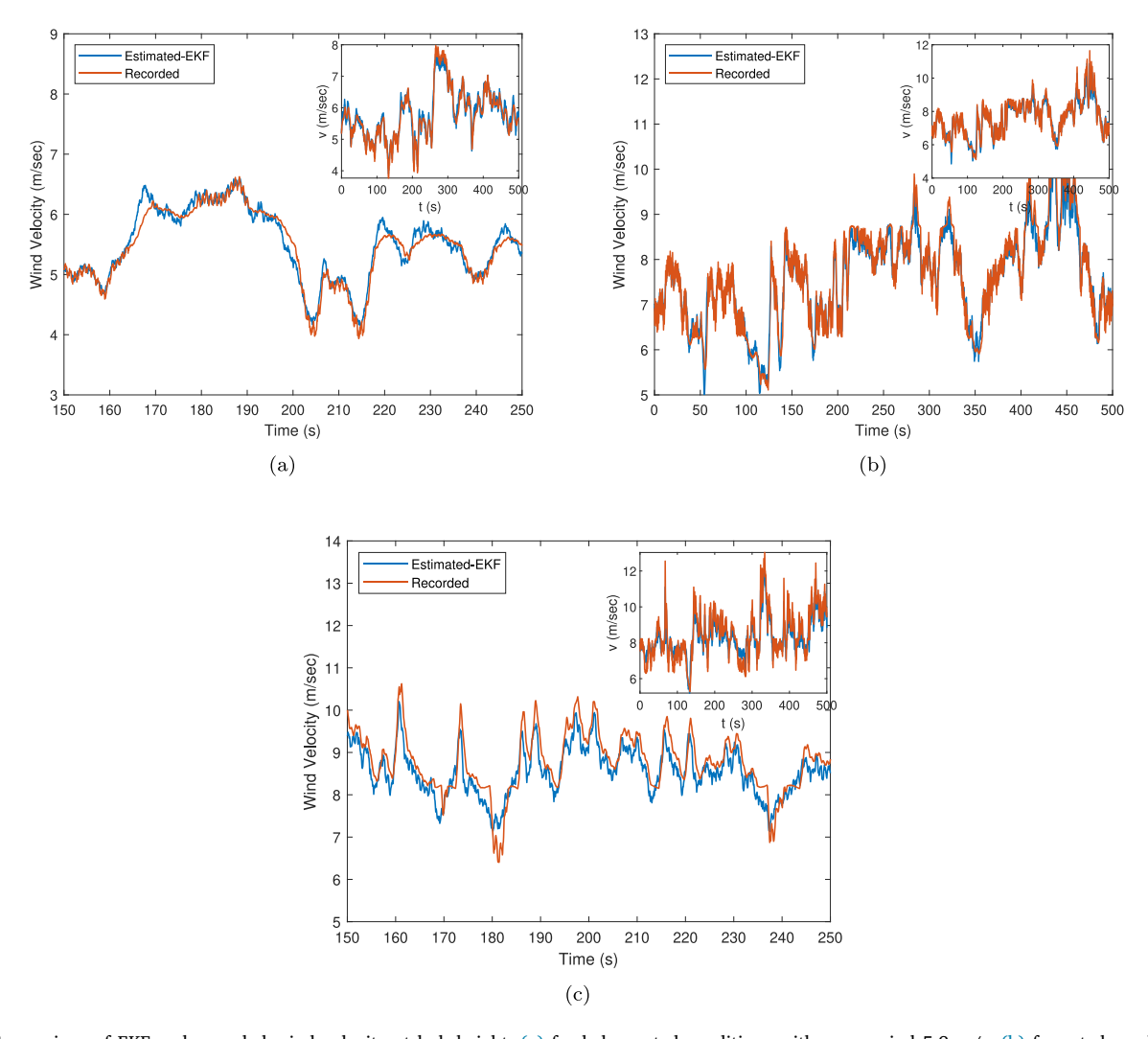


Fig. 15. Comparison of EKF and recorded wind velocity at hub height; (a) for below-rated conditions with mean wind 5.9 m/s, (b) for rated conditions with mean wind 7.9 m/s (c) for rated conditions with mean wind 9.2 m/s.

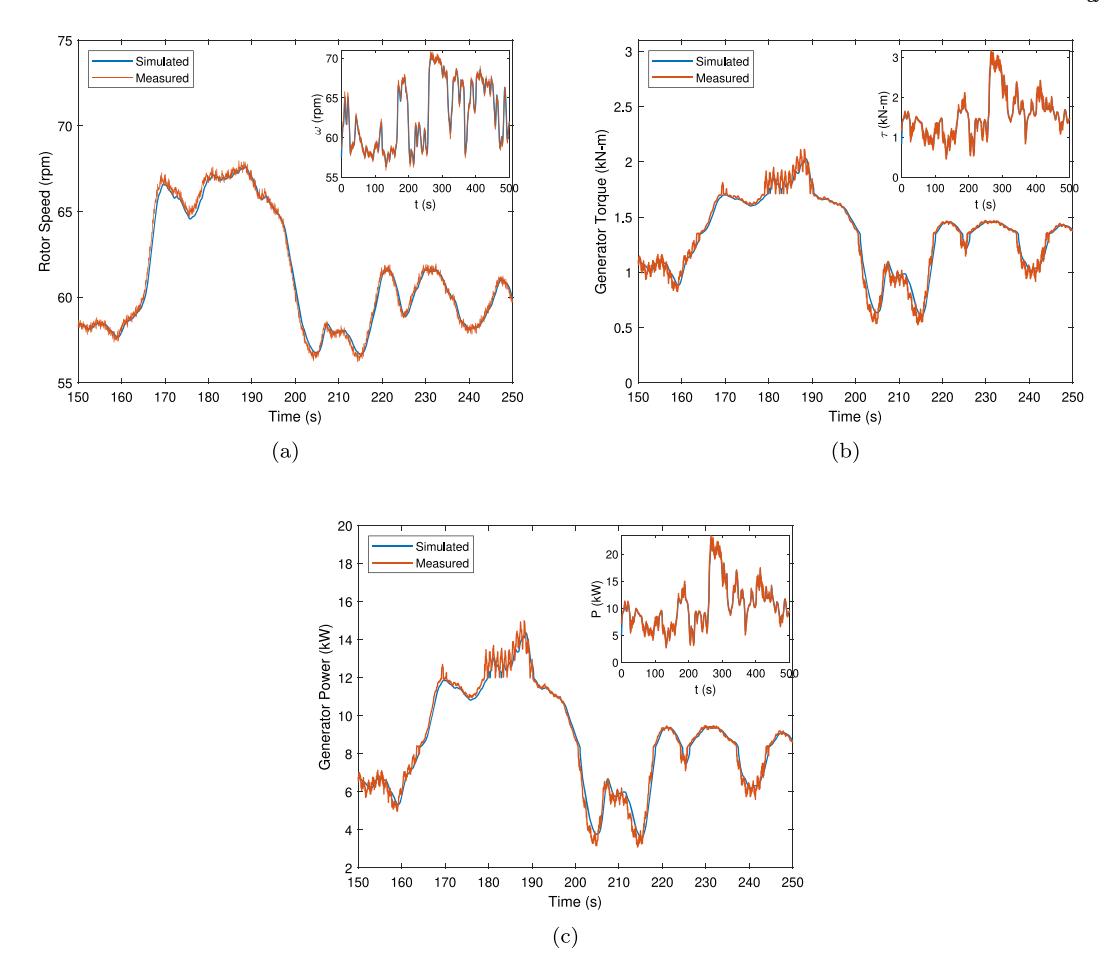


Fig. 16. Response comparison between "simulated" (using openFAST) and "measured" (field measurements) responses for below-rated conditions with mean wind 5.9 m/s; (a) Rotor Speed, (b) Generator Torque, (c) Generator Power.

 Table 8

 Simulated and measured turbine response comparison.

Mean wind (m/s)	5.9			7.9		9.2	
Responses		Measured	Simulated	Measured	Simulated	Measured	Simulated
Potential (man)	μ	62.83	62.82 [0.02]	70.08	70.01 [0.10]	72.83	72.64[0.26]
Rotor speed (rpm)	σ	4.06	4.08 [0.49]	2.88	2.91[1.04]	2.91	2.92 [0.34]
Comparator toward (I-N)	μ	1.55	1.54 [0.65]	2.96	2.93 [1.01]	3.09	2.93 [5.17]
Generator torque (kN-m)	σ	0.51	0.52 [1.96]	0.79	0.80[1.26]	0.39	0.42 [7.69]
Constant and Carlo	μ	10.41	10.39 [0.19]	21.91	21.69 [1.01]	23.58	22.51[4.53]
Generator power (kW)	σ	4.08	4.15 [1.71]	6.39	6.52 [2.03]	2.69	2.89 [7.43]

N.B.:The values within [.] indicate the percentage error between measured and simulated turbine responses.

speed is estimated directly from the electrical power using the following expression

$$\hat{v}_{est} = \sqrt[3]{\frac{2P_{el}}{\rho AC_p(\lambda, \beta)}} \tag{5}$$

where P_{el} is the measured electrical power, the power coefficient $C_p(\lambda,\beta)$ is calculated from the measured rotor speed and blade pitch angle, and the estimated wind speed \hat{v}_{est} fed back to Eq. (5).

In the second method, for inverse characterization and comparison, the rotor effective wind speed is also estimated using an extended Kalman filter (EKF). For this purpose, the wind speed estimator used in ROSCO [38] for the TSR tracking generator torque controller and pitch saturation routines is used in this study. The choice of the standard EKF for this paper is based on the fact that the EKF has demonstrated sufficient accuracy in estimating the rotor average effective wind speeds in previous studies. The interested reader is referred to the following

papers on the comparison of different real-time wind speed estimation techniques [71–73] The wind speed estimate \hat{v}_k can be expressed as $\hat{v}_k = (v_t + v_m)$, where v_t and v_m are the turbulent and the mean component of wind speed, respectively.

The nonlinear state-space wind estimator model and measurement equations used in the EKF-based updating algorithm are given by

$$\dot{x} = f(x, u) + g_s \tag{6a}$$

$$y = h(x, u) + g_m = \omega_r + g_m \tag{6b}$$

where f(x|u) and h(x,u) are the nonlinear state transition and output functions, respectively. In these equations, the model noise $g_s = [n_1 n_2 n_3]^T$ and the measurement noise g_m are assumed to be Gaussian white noise with a finite covariance. The state and input vectors are denoted by $x = [\omega_r v_t v_m]^T$, and $u = [\theta \quad \tau_g]$, respectively. Blade pitch angle and generator torque are assumed to be noise-free inputs and are directly obtained from their respective measurements. The nonlinear

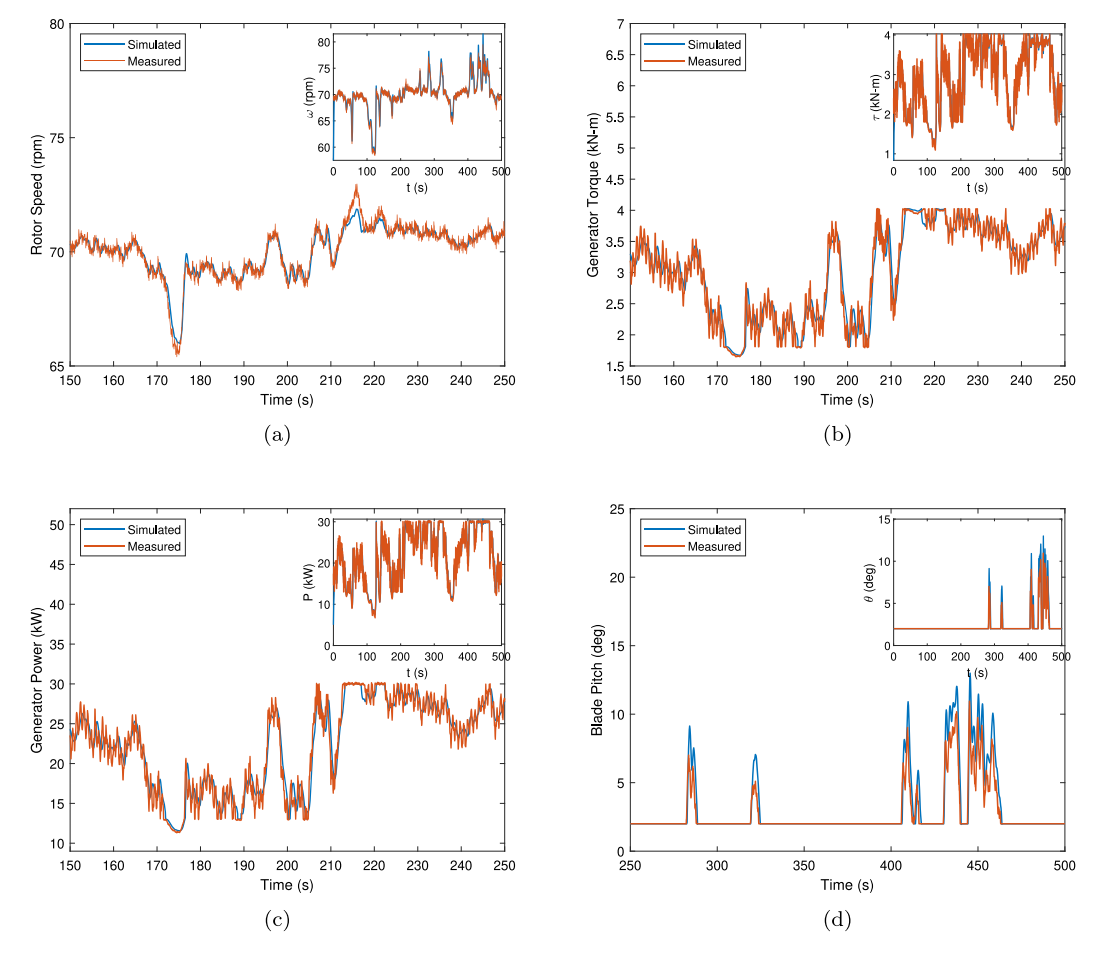


Fig. 17. Response comparison between "simulated" (using openFAST) and "measured" (field measurements) responses for rated operating condition with mean wind 7.9 m/s; (a) Rotor Speed, (b) Generator Torque, (c) Generator Power, (d) Blade Pitch.

state space equations for the EKF-based identification are given by

$$\dot{\omega}_r = \frac{1}{I} \left(\tau_a - N_g \tau_g \right) \tag{7a}$$

$$\dot{v}_t = -\frac{\pi v_m}{2L} v_t + n_1 \tag{7b}$$

$$\dot{v}_m = n_2 \tag{7c}$$

where ω_r is the rotor speed, J is the rotor inertia, N_g is the gearbox ratio, and τ_g is the generator torque. L_t is a turbulence length scale parameter generically defined as $L_t=3D$, where D is the rotor diameter. In this model the aerodynamic torque τ_a can be calculated as

$$\tau_a = 0.5 \rho A C_p(\lambda, \theta) \hat{v}^3 \omega_r^{-1} \tag{8}$$

In Eq. (8), ρ is the air density, A is the rotor area, θ is the blade pitch angle, and λ is the tip speed ratio, i.e., $\lambda = \frac{\omega_P R}{\delta}$. A second-order central differencing approach calculates the Cp surface gradients at operating points.

The process noise (Q) and measurement noise (R_m) covariances in the EKF algorithm are considered as per [37], which are given by

$$Q = \begin{pmatrix} 10^{-5}0 & 0 & & \\ 0 & \frac{\pi v_m^3 t_i^2}{L} & 0 & \\ 0 & 0 & \frac{2^2}{500} \end{pmatrix}, R_m = 0.02$$
 (9)

The turbulence intensity is considered as $t_i = 0.18$, the upper zone of the turbulence intensity for standard inflow wind conditions as defined by [74]. Therefore, the state estimation for the prediction step in the

EKF algorithm uses the following equation

$$\dot{x}(t) = f\left(x_{k-1|k-1}, u_k\right) \tag{10}$$

In this algorithm the predicted covariance estimate is given by

$$\dot{P}(t) = F(t) P_{k|k} + P_{k|k} F^{T}(t) + Q_k - K_{k-1} R_m K_{k-1}^{T}$$
(11)

It may be noted that the Kalman gain (K_k) is computed as

$$K_k = P_{k|k-1} J_k^T [J_k P_{k|k-1} J_k^T + R_m]^{-1}$$
(12)

Where the Jacobians corresponding to the measurement equations are defined as $F(t) = \left. \frac{\partial f}{\partial x} \right|_{x_{k-1|k-1}, u_k}$, and $J_k = \left. \frac{\partial h}{\partial x} \right|_{x_{k|k-1}}$, respectively. Once the state prediction is completed, the measurement is updated as

$$\tilde{y}_k = y_k - h_k(x_{k|k-1}) \tag{13}$$

It is followed by state updation using updated measurement \tilde{y}_k , which is given by

$$x_{k|k} = x_{k|k-1} + K_k \tilde{y}_k \tag{14}$$

Finally, the covariance is updated as follows

$$P_{k|k} = (I - K_k J_k) P_{k|k-1}$$
(15)

Once the state is updated at the k^{th} time instance, the rotor effective wind speed is then estimated as follows

$$\hat{v}_k = [0 \ 1 \ 1] x_{k|k} \tag{16}$$

Using the above-mentioned wind estimator, the rotor effective wind speed time history is evaluated for three operating conditions discussed earlier. Fig. 15 shows the details of these estimated time histories,

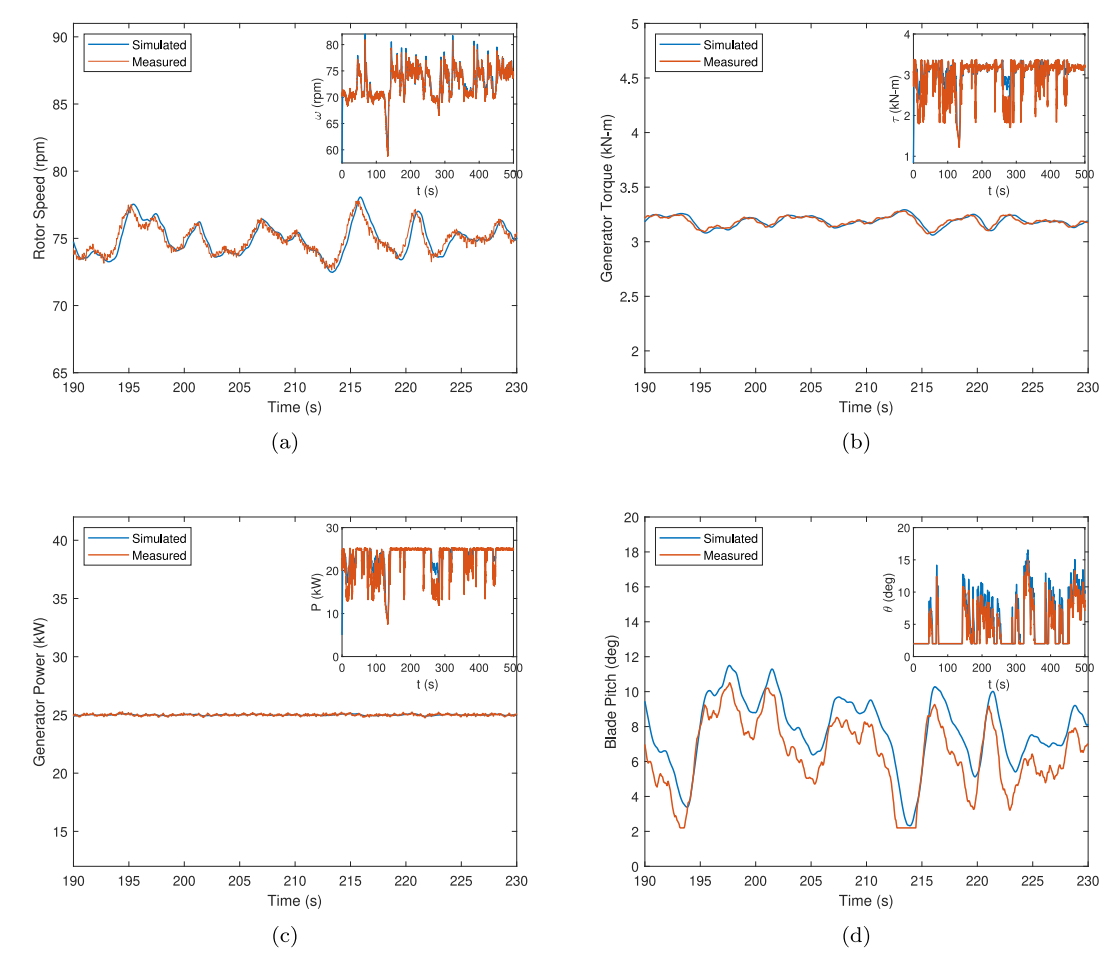


Fig. 18. Response comparison between "simulated" (using openFAST) and "measured" (field measurements) responses for above-rated conditions with mean wind 9.2 m/s; (a) Rotor Speed, (b) Generator Torque, (c) Generator Power, (d) Blade Pitch.

which closely match the measured speed, indicating the accuracy of the EKF-based model updating. Furthermore, the relative root mean square (RRMS) error and Time Response Assurance Criteria (TRAC) for these three cases are estimated using the following expressions

$$RRMSE = \sqrt{\frac{(y - \hat{y})^T (y - \hat{y})}{y^T y}}$$
 (17a)

$$TRAC = \frac{(y^T \hat{y})^2}{(y^T y)(\hat{y}^T \hat{y})}$$
 (17b)

The values of these model indicators are highlighted in Table 7. The estimated relative error values, i.e., RRMS, are mostly well within 10%, indicating an accurate estimation of these parameters. Besides RRMS of error, TRAC values are also presented in the same table, which indicates the degree of correlation between the measured and modeled responses. The values of this indicator are more than 99% in all the cases, supporting the accuracy of the updated model.

6. Model validation

In this section, the OpenFAST model of the test turbine is validated. Firstly, a comprehensive description of the turbine model implemented in OpenFAST [44] is provided. Following this, the turbine's performance is validated by comparing its key performance indicators, specifically rotor speed, generator torque, generator power, blade pitch operations, and tower base moments, with field measurements under three operational conditions, as outlined in Section 4. These comparisons are made using the estimated wind speeds described in the previous Section to ensure a rigorous evaluation. Lastly, an analysis of the tower and

blades' steady-state responses is included, demonstrating their behavior as functions of wind speeds. This analysis offers a comprehensive insight into the overall dynamics of the turbine components.

6.1. Turbine response validation

The National Renewable Energy Laboratory's (NREL) OpenFAST is a popular tool for wind turbine aerodynamics and dynamic simulation. It uses a primary input file to describe the wind turbine operating parameters and basic geometry. However, the blade, tower, and aerodynamic parameters and wind-time histories are read from separate files. The layout of the mode of operation, along with the detailed descriptions of individual input files, are provided in [5]. For the current study, the ADAMS post-processor is not employed. This study adopts the estimated rotor effective wind realizations in the InflowWind [75] module and are applied as uniform wind fields at hub height. Finally, the baseline torque and pitch control parameters are delineated through a dynamic link library (DLL) interface described in Section 3.

The simulated turbine responses for the three different operating conditions, as described in Section 4, are shown in Figs. 16 to 18. The comparisons of different performance parameters are listed in Table 8. The numerical figures presented in this table show that the mean and standard deviation of rotor speed, generator torque, and generator power remain within 2% except at 9.22 m/s, where the difference is around 5 to 7% (i.e., <10%). In addition to the key turbine parameters, Figs. 17(d) and 18(d) also show the variable pitch time histories applied in two different cases, i.e., test setup and updated OpenFAST model. The minor discrepancies between the simulated and measured pitch

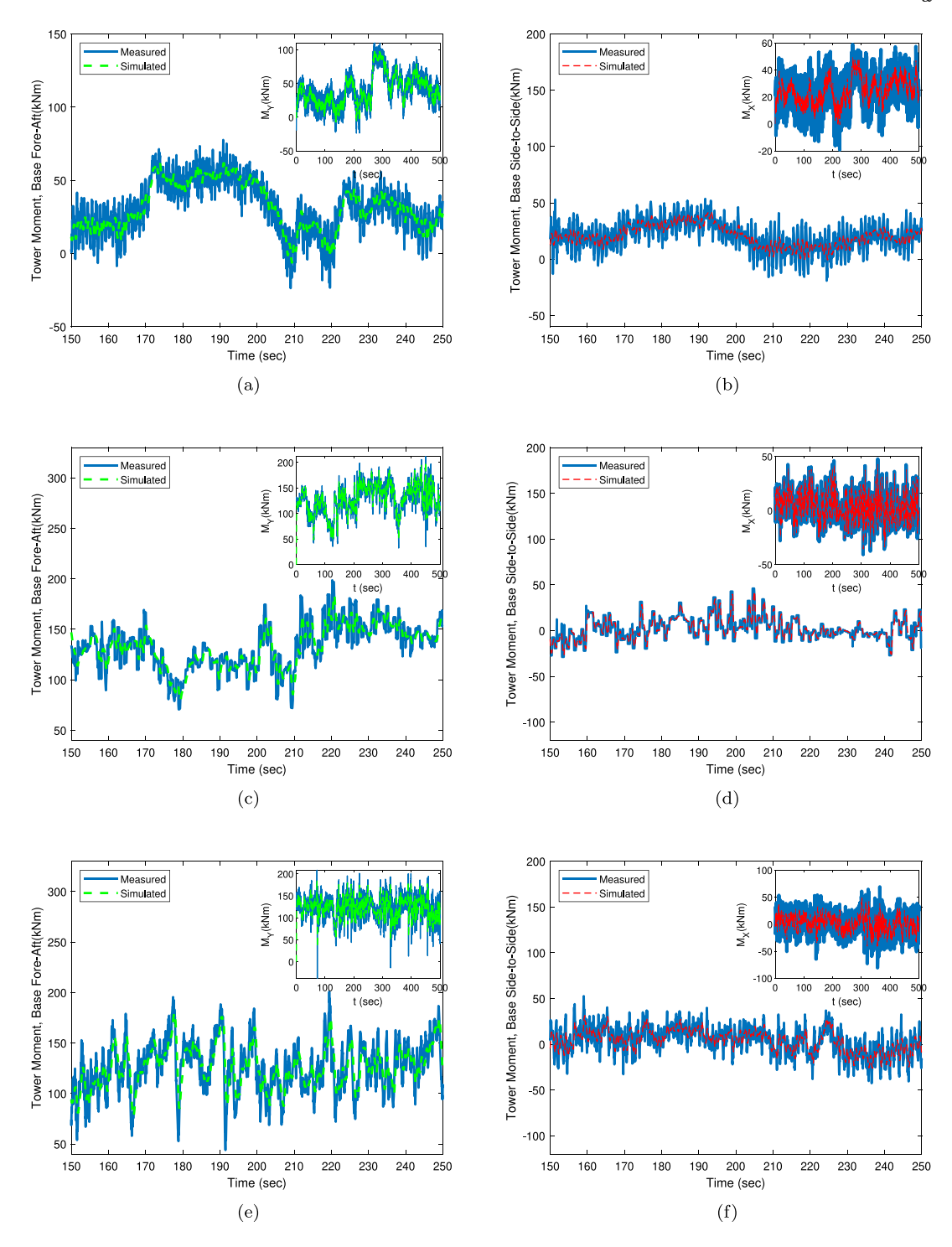


Fig. 19. Response comparison between simulated and actual tower base measurements; (a) FA moment with mean wind 5.9 m/s, (b) SS moment with mean wind 5.9 m/s, (c) FA moment with mean wind 7.9 m/s, (d) SS moment with mean wind 7.9 m/s (e) FA moment with mean wind 9.2 m/s, (f) SS moment with mean wind 9.2 m/s.

may be attributed to several factors - (i) improper quantification of the measurement error, (ii) use of aerodynamic power coefficient (Cp) based on steady wind flow conditions as a general practice (as opposed to turbulent flow in reality), (iii) unmodeled pitch actuator dynamics. These aspects will be investigated in subsequent works.

6.2. Tower responses validation

Further, the tower base moments are validated to demonstrate the accuracy of the benchmark model. The strain sensors in the steel base are considered for these measurements. Moment equations are

systematically derived from the test data documented in [45]. The foreaft and side-to-side moments are derived based on nacelle orientation and transformations. In this formulation, the effect of temperature is ignored, while the wind direction and yaw bearing position are considered for meaningful moment estimation. This conversion of strains into moments using different measurements is bound to have inherent errors. On the other hand, the simulated moments are based on a multi-body dynamic model having some modeling error no matter how accurate it may be. Hence, Kalman-based updating is adopted here to minimize the error between the measurement and simulation, which

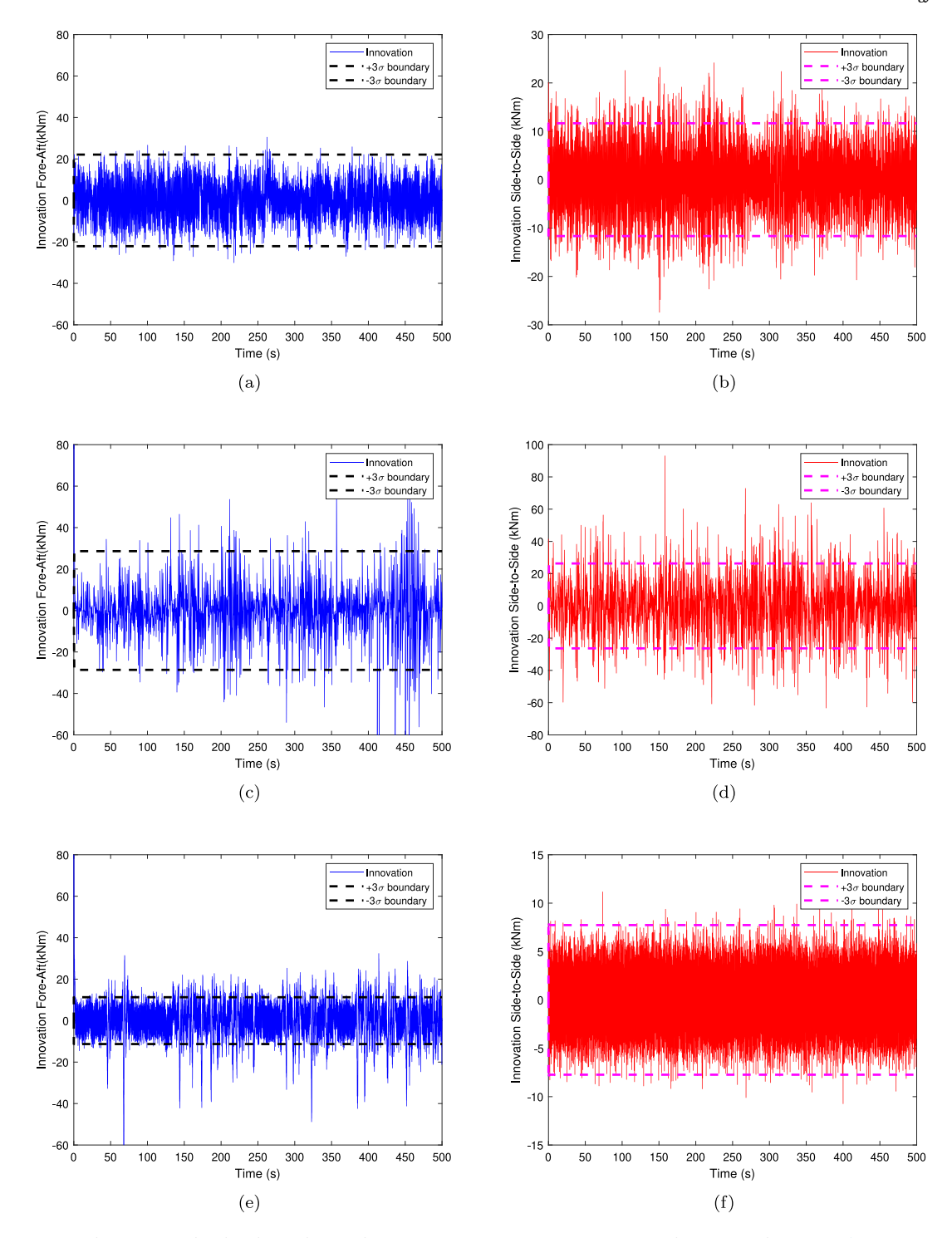


Fig. 20. Estimation error between simulated and actual tower base measurements; (a) FA innovations with mean wind 5.9 m/s, (b) SS innovations with mean wind 5.9 m/s, (c) FA innovations with mean wind 7.9 m/s, (d) SS innovations with mean wind 7.9 m/s (e) FA innovations with mean wind 9.2 m/s, (f) SS innovations with mean wind 9.2 m/s.

can be expressed as follows.

$$x_{k+1} = Ax_k + w_k \tag{18}$$

$$z_k = Hx_k + v_k \tag{19}$$

Where x_k represents the state vector at time step k (simulated fore-aft and side-to-side moments), and z_k represents the measurement vector at time step k (i.e., fore-aft and side-to-side moments). A and H are the state transition and the observation matrix. w_k is the process noise vector, assumed to be Gaussian with zero mean and covariance Q, and v_k is the measurement noise vector with covariance R. The covariance

R is chosen based on the quality of the measurement and defined as $R = diag(v_{FA}, v_{SS})$, where v_{FA} and v_{SS} are noise covariances of tower base fore-aft and side-to-side measured moments, respectively. Typically, these noise covariance are approximately 5% to 10% of the variance of the measurements. In this study, this covariance is initiated with 10% of the variance of the measurements. The Kalman algorithm is then implemented through the following steps.

Time Update (Prediction):

$$\hat{x}_{k+1|k} = A\hat{x}_{k|k} \tag{20}$$

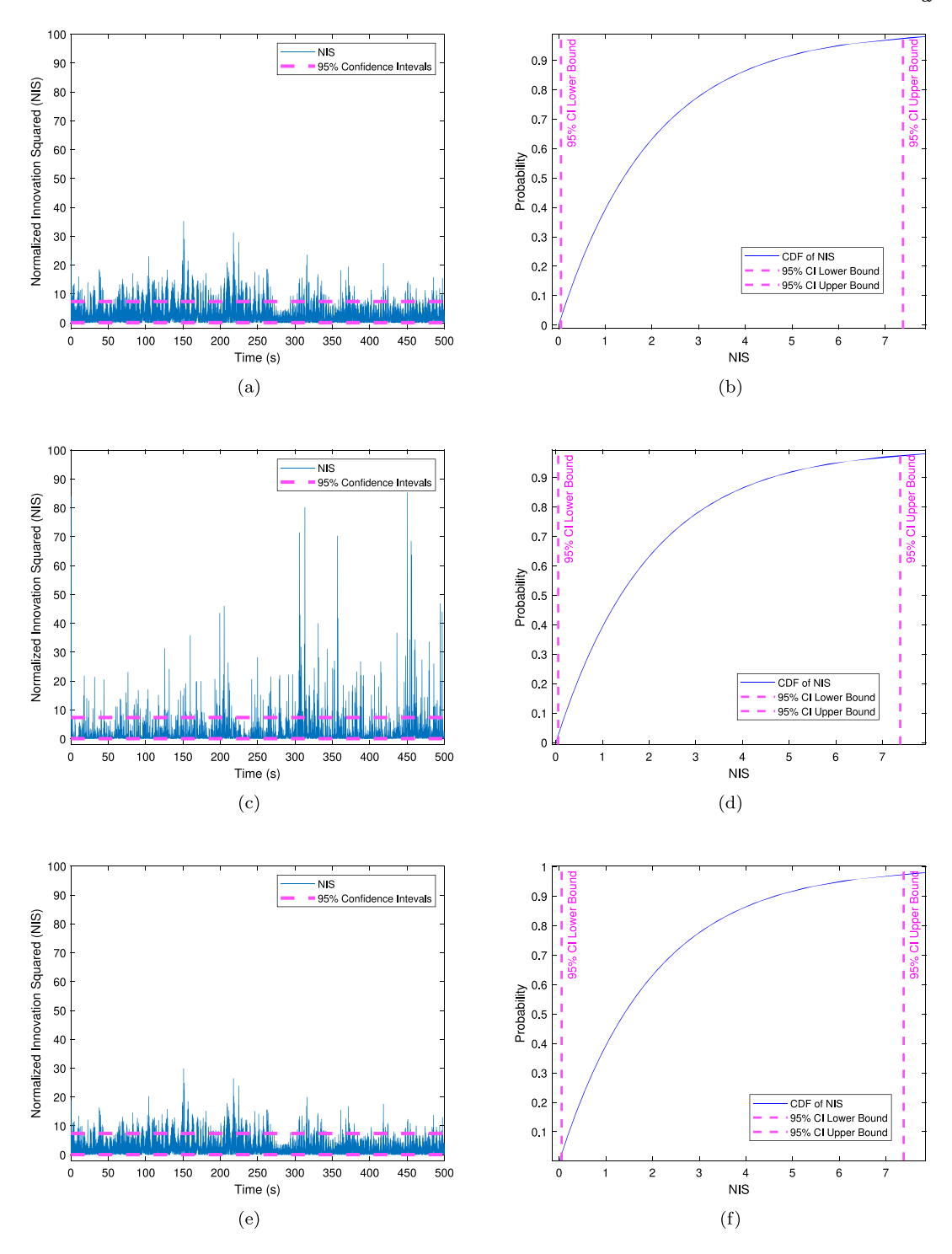


Fig. 21. Normalized innovation squared test; (a) NIS with mean wind 5.9 m/s, (b) CDF of NIS with mean wind 5.9 m/s, (c) NIS with mean wind 7.9 m/s, (d) CDF of NIS with mean wind 7.9 m/s, (e) NIS with mean wind 9.2 m/s, (f) CDF of NIS with mean wind 9.2 m/s.

$$P_{k+1|k} = A P_{k|k} A^T + Q (21)$$

Measurement Update (Correction):

$$K_{k+1} = P_{k+1|k} H^{T} (H P_{k+1|k} H^{T} + R)^{-1}$$
(22)

$$\hat{x}_{k+1|k+1} = \hat{x}_{k+1|k} + K_{k+1}(z_{k+1} - H\hat{x}_{k+1|k})P_{k+1|k}$$
 (23)

$$P_{k+1|k+1} = (I - K_{k+1}H)P_{k+1|k}$$
(24)

The simulated and measured tower root moments for the three different operating conditions, as described in Section 4, are presented in Figs.

19. The comparison plots demonstrate the closeness of the simulated and measured tower base moments.

The Kalman filter is tuned statistically based on the estimation error between the system states $(x_k - \hat{x}_k)$ and the error between measurements $e_k = (z_k - H\hat{x}_k)$, which are Gaussian and white. In other words, the statistics of the state and measurement errors should be consistent with the chosen covariances Q and R [76]. Since the true system state x_k is often hard to obtain, filter tuning is typically done by examining the measurement errors e_k , also known as innovation. By definition of a well-tuned filter, the innovation sequence e_k should have a zero mean, and approximately 99.7% of the innovations should be

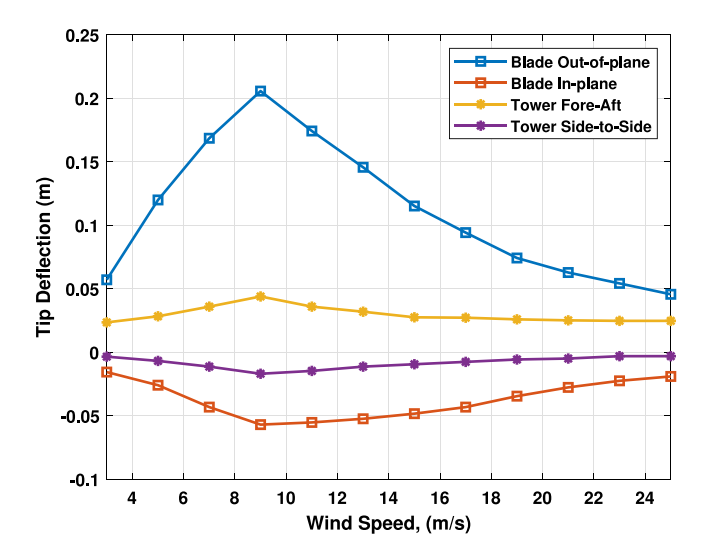


Fig. 22. Steady state response of tower and blade.

bounded within $\pm 3\sigma$ where the innovation covariance matrix at time step k is defined as $S_k = HP_kH^T + R$. The fore-aft and side-to-side innovations and their $\pm 3\sigma$ boundaries for the three different operating scenarios are shown in Fig. 20. Further, to satisfy the Gaussian assumption of the innovation sequences, two innovation sequences in this study can be normalized into one quantity. That is the normalized innovation squared (NIS), denoted as $v_k = e_k^T S_k^{-1} e_k$. For a well-tuned filter, the normalized innovation squared is expected to be Chi-squared distributed with n degrees of freedom $(v_k \sim \chi_n^2)$. In other words, the normalized innovation squared must lie within the confidence interval $v_k \in \left[F_X^{-1}\left(\frac{\alpha}{2}, n\right), F_X^{-1}\left(1 - \frac{\alpha}{2}, n\right)\right]$, where F^{-1} is the inverse cumulative distribution function of the Chi-squared distribution. In this case, the number of measurements is n = 2; thus, the upper and lower bounds are $\left[F_X^{-1}(0.025, 2), F_X^{-1}(0.975, 2)\right] = [0.05, 7.38]$ with $\alpha = 0.05$ (two-sided 95% confidence interval). Fig. 21 shows most of the normalized innovation squared lies within the confidence intervals, and the right plot shows the cumulative distribution of the normalized innovation squared ν . Thus, the hypothesis is acceptable, and the innovation sequences e_{k} are unbiased Gaussian distributed, as shown in Fig. 21.

6.3. Steady-state behavior of tower and blade

Once the model was validated satisfactorily, further effort was made to investigate the steady-state performance envelope of the tower and blade. For this purpose, different steady wind fields are generated using TurbSim [77]. Using these wind fields, the updated model of the turbine is simulated, and the peak performance curve for tower and blade tip response in two orthogonal directions at different mean wind speeds are presented in Fig. 22. The out-of-plane tip deflection of the blade (Blade 1) reaches a maximum at the rated operating point before dropping again. This response characteristic results from the rotor thrust attaining peak value at the rated speed. This feature is typical of a wind turbine with a variable pitch rotor because of the transition in the control system at rated between the active generator-torque and the active blade-pitch control regions. This behavior is also visible in the in-plane tip deflection of the blade and the tower-top fore-aft and side-to-side displacement.

7. Conclusions

This paper presents an inverse identification of the Chalmers Wind Turbine [78], which is a small-scale horizontal-axis wind turbine. The paper presents a detailed procedure for inverse identification and provides a benchmarked model of the Chalmers small-scale wind turbine

to the wind energy community for research and development. Please note that the Chalmers Wind Turbine is one of the listed facilities under the EAWE Test Wind Turbines Committee (TWTC) [79], which provides direct access to all measurements. These research turbines are essential for understanding the behavior of wind and wind turbines in research and education. Therefore, benchmarking the numerical model of the Chalmers Wind Turbine against field measurements is a big step forward in this direction. The paper's contribution is broken down as follows.

- The main aim of this study is to focus on the system characterization of a small onshore horizontal-axis test turbine. It is achieved through rigorous testing of the tower, followed by finite element modeling of these components. The modal characteristics of these components are also identified through signal processing of measurements from the combined tower-drive train-rotor assembly operating under different wind flow conditions. The wavelet-based signal processing successfully identifies the modal parameters of the tower and the blades with a significant level of accuracy when compared with the detailed FE model. This system characterization, encompassing every level (i.e., local features to global behavior), using turbines in various operating conditions, has not been attempted in the literature earlier.
- The wind flow model used to estimate the rotor effective wind speed proposed by [37], incorporating power and control parameters, is adopted in this study. Abbas et al. [38] also used this model to develop the ROSCO controller for TSR tracking generator torque control, adopting simulated hypothetical benchmark turbines. However, the performance of this model was never tested using actual data under different operating conditions, which is attempted here. This is achieved through an EKF-based filtering algorithm. The rotor effective wind speed is tracked in real-time using the actual measurements, i.e., rotor speed, generator torque, and power output. The numerical results presented in this paper highlight the accuracy of the wind estimation process. The relative error estimates and correlation of the modeled turbine response with measurement indicate the robustness of the wind flow model, which can be further utilized for turbine response analysis and design.
- · Finally, the complete description of the multi-body dynamic model in OpenFAST is presented here. This can serve as the benchmark for further studies on modeling, analysis, and controller design, among many other aspects of horizontal-axis wind turbines. In this context, it is worth noting that all other benchmark models available in the literature are based mainly on code-to-code comparisons and validations. In contrast, the benchmark model of the 45 kW turbine presented in this paper is based entirely on the actual test bed. The simulated responses of the model turbine are compared with exact measurements, including rotor speed, generator power, generator torque, blade pitch angle, and tower base moments. These simulated results closely match the measurement, confirming the accuracy of the multi-body dynamic model. Finally, the steady-state responses of the tower and blade as a function of wind speed are also included for further studies on this topic.

In summary, this paper focuses on the validation of the multibody dynamic modeling and analysis of horizontal-axis wind turbines. Although a complete description of the HAWT and the wind flow model is presented here with significant emphasis on the key turbine parameters, i.e., rotor speed, generator power, generator torque, blade pitch angle, and tower base moments, the blade response is not covered in this paper except for a few basic features. The authors wish to cover these details, i.e., aeroelastic behavior, aero-dynamic damping estimation, and transient blade responses operating in a closed-loop control network, in their future communications, as accommodating all these details in a single paper is complex.

CRediT authorship contribution statement

Debasis Panda: Visualization, Validation, Software, Methodology, Investigation, Formal analysis, Conceptualization. **Arunasis Chakraborty:** Writing – review & editing, Supervision, Methodology, Investigation, Formal analysis, Conceptualization. **Saptarshi Sarkar:** Writing – review & editing, Writing – original draft, Supervision, Project administration. **Håkan Johansson:** Writing – review & editing, Supervision, Conceptualization.

Declaration of competing interest

The authors declare the following financial interests/personal relationships which may be considered as potential competing interests: Debasis Panda reports financial support was provided by Government of India. If there are other authors, they declare that they have no known competing financial interests or personal relationships that could have appeared to influence the work reported in this paper.

Acknowledgments

The authors greatly acknowledge the contribution of Sara Fogel-ström and Prof Ola Carlson from the Department of Electrical Engineering, Chalmers University of Technology, Sweden in setting up the aeroelastic model of the Chalmers research wind turbine. The Chalmers research wind turbine has been erected with support from the Swedish Wind Power Technology Centre, the Swedish Energy Agency, Sweden, and the Region of Västra Götaland, Sweden. The main purpose of the turbine is to foster wind power research. The wooden tower is a collaboration with Modvion to test the feasibility of wood as a material in wind turbines. The turbine is also available in the EAWE Test Wind Turbines Committee space.

The first author acknowledges the Ministry of Education, Govt. of India, for the Prime Minister Research Fellowship (PMRF ID: 1902715) to support this work.

Data availability

The multi-body model of the turbine and the data supporting the findings of this work are available from the corresponding author upon reasonable request.

References

- J.M. Jonkman, Modeling of the UAE Wind Turbine for Refinement of FAST_AD, Tech. Rep., National Renewable Energy Lab, Golden, CO (US), 2003.
- [2] C. Bak, F. Zahle, R. Bitsche, T. Kim, A. Yde, L.C. Henriksen, M.H. Hansen, J.P.A.A. Blasques, M. Gaunaa, A. Natarajan, The DTU 10-MW reference wind turbine, in: Danish Wind Power Research 2013, 2013.
- [3] E. Gaertner, J. Rinker, L. Sethuraman, F. Zahle, B. Anderson, G. Barter, N. Abbas, F. Meng, P. Bortolotti, W. Skrzypinski, et al., Definition of the IEA 15-Megawatt Offshore Reference Wind Turbine, National Renewable Energy Laboratory (NREL), 2020.
- [4] K.L. Dykes, J. Rinker, Windpact Reference Wind Turbines, Tech. Rep., National Renewable Energy Lab.(NREL), Golden, CO (United States), 2018.
- [5] J.M. Jonkman, M.L. Buhl Jr., et al., FAST User's Guide, Tech. Rep., National Renewable Energy Lab.(NREL), Golden, CO (United States), 2005.
- [6] M. Rezaei, H. Zohoor, H. Haddadpour, Aeroelastic modeling and dynamic analysis of a wind turbine rotor by considering geometric nonlinearities, J. Sound Vib. 432 (2018) 653–679.
- [7] Z. Xue, W. Wang, L. Fang, J. Zhou, Numerical simulation on structural dynamics of 5 MW wind turbine, Renew. Energy 162 (2020) 222–233, http://dx.doi.org/ 10.1016/j.renene.2020.08.028.
- [8] A. Mitra, A. Chakraborty, Multi-objective optimization of composite airfoil fibre orientation under bending-torsion coupling for improved aerodynamic efficiency of horizontal axis wind turbine blade, J. Wind. Eng. Ind. Aerodyn. 221 (2022) 104881, http://dx.doi.org/10.1016/j.jweia.2021.104881.

- [9] S. Liu, Q. Li, B. Lu, J. He, Analysis of NREL-5MW wind turbine wake under varied incoming turbulence conditions, Renew. Energy 224 (2024) 120136, http://dx.doi.org/10.1016/j.renene.2024.120136.
- [10] S. Sarkar, A. Chakraborty, Development of semi-active vibration control strategy for horizontal axis wind turbine tower using multiple magneto-rheological tuned liquid column dampers, J. Sound Vib. 457 (2019) 15–36, http://dx.doi.org/10. 1016/j.jsy.2019.05.052.
- [11] M.A. Abdelbaky, X. Liu, Di Jiang, Design and implementation of partial offline fuzzy model-predictive pitch controller for large-scale wind-turbines, Renew. Energy 145 (2020) 981–996, http://dx.doi.org/10.1016/j.renene.2019.05.074.
- [12] S. Sarkar, L. Chen, B. Fitzgerald, B. Basu, Multi-resolution wavelet pitch controller for spar-type floating offshore wind turbines including wave-current interactions, J. Sound Vib. 470 (2020) 115170, http://dx.doi.org/10.1016/j.jsv. 2020.115170.
- [13] R. Hu, C. Le, Z. Gao, H. Ding, P. Zhang, Implementation and evaluation of control strategies based on an open controller for a 10 MW floating wind turbine, Renew. Energy 179 (2021) 1751–1766, http://dx.doi.org/10.1016/j.renene.2021.07.117.
- [14] M.M. Sajeer, A. Mitra, A. Chakraborty, Spinning finite element analysis of longitudinally stiffened horizontal axis wind turbine blade for fatigue life enhancement, Mech. Syst. Signal Process. 145 (2020) 106924, http://dx.doi.org/ 10.1016/j.vmssp.2020.106924.
- [15] Y. Yang, M. Bashir, C. Michailides, X. Mei, J. Wang, C. Li, Coupled analysis of a 10 MW multi-body floating offshore wind turbine subjected to tendon failures, Renew. Energy 176 (2021) 89–105, http://dx.doi.org/10.1016/j.renene.2021.05. 079.
- [16] W. Chai, L. He, W. Chen, L. Cao, W. Shi, C. Sinsabvarodom, M. Hu, Z. Liu, Short-term extreme value prediction for the structural responses of the IEA 15 MW offshore wind turbine under extreme environmental conditions, Ocean Eng. 306 (2024) 118120, http://dx.doi.org/10.1016/j.oceaneng.2024.118120.
- [17] J. Liang, Y. Fu, Y. Wang, J. Ou, Identification of equivalent wind and wave loads for monopile-supported offshore wind turbines in operating condition, Renew. Energy 237 (2024) 121525, http://dx.doi.org/10.1016/j.renene.2024.121525.
- [18] IEA Wind, IEA wind task 27: Small wind turbines in turbulent sites, 2025, https://community.ieawind.org/task27/27workplan. (Accessed 7 June 2025).
- [19] IEA Wind, IEA wind task 41: Enabling wind to contribute to a sustainable future energy system, 2025, https://ieawind.org/task41. (Accessed 7 June 2025).
- [20] T. Kijewski, Wavelet transforms for system identification: considerations for civil engineering applications, Comput. Aided Civ. Infrastruct. Engineering-an Int. J. 18 (2003) 341–357.
- [21] Q. Li, J. Wu, Time-frequency analysis of typhoon effects on a 79-storey tall building, J. Wind Eng. Ind. Aerodyn. 95 (12) (2007) 1648–1666.
- [22] A. Chakraborty, B. Basu, M. Mitra, Identification of modal parameters of a mdof system by modified L-P wavelet packets, J. Sound Vib. 295 (3-5) (2006) 827-837.
- [23] H. Wang, J. Mao, J. Huang, A. Li, Modal identification of Sutong cable-stayed bridge during typhoon haikui using wavelet transform method, J. Perform. Constr. Facil. 30 (5) (2016) 04016001.
- [24] P. Murtagh, B. Basu, Identification of equivalent modal damping for a wind turbine at standstill using Fourier and wavelet analysis, Proc. Inst. Mech. Eng. Part K: J. Multi-Body Dyn. 221 (4) (2007) 577–589.
- [25] B. Chen, Z. Zhang, X. Hua, B. Basu, S.R. Nielsen, Identification of aerodynamic damping in wind turbines using time-frequency analysis, Mech. Syst. Signal Process. 91 (2017) 198–214.
- [26] W. Teng, X. Ding, X. Zhang, Y. Liu, Z. Ma, Multi-fault detection and failure analysis of wind turbine gearbox using complex wavelet transform, Renew. Energy 93 (2016) 591–598, http://dx.doi.org/10.1016/j.renene.2016.03.025.
- [27] C. Yi, Z. Yu, Y. Lv, H. Xiao, Reassigned second-order Synchrosqueezing transform and its application to wind turbine fault diagnosis, Renew. Energy 161 (2020) 736–749, http://dx.doi.org/10.1016/j.renene.2020.07.128.
- [28] A. Mitra, Y. Giridharan, A. Chakraborty, Wavelet linear quadratic regulator-based gain scheduling for optimal fore-aft vibration control of horizontal axis wind turbine tower using active tuned mass damper, Struct. Control. Heal. Monit. 29 (11) (2022) e3055.
- [29] D. Schlipf, P.W. Cheng, Robust wind turbine state and wind parameter estimation using Kalman filtering, Wind. Energy 17 (5) (2014) 655–674, http://dx.doi.org/ 10.1002/we 1610
- [30] D. Zou, H. Zhao, G. Liu, N. Ta, Z. Rao, Application of augmented Kalman filter to identify unbalance load of rotor-bearing system: Theory and experiment, J. Sound Vib. 463 (2019) 114972, http://dx.doi.org/10.1016/j.jsv.2019.114972.
- [31] Y. Lei, H. Qiu, F. Zhang, Identification of structural element mass and stiffness changes using partial acceleration responses of chain-like systems under ambient excitations, J. Sound Vib. 488 (2020) 115678, http://dx.doi.org/10.1016/j.jsv. 2020.115678.
- [32] D. Wei, D. Li, T. Jiang, P. Lyu, X. Song, Load identification of a 2.5 MW wind turbine tower using Kalman filtering techniques and BDS data, Eng. Struct. 281 (2023) 115763, http://dx.doi.org/10.1016/j.engstruct.2023.115763.
- [33] A. Mehrjoo, E.M. Tronci, B. Moaveni, E. Hines, Hybrid surrogate input load estimation model in offshore wind turbines using transfer learning and multitask learning, Renew. Energy (2025) http://dx.doi.org/10.1016/j.renene.2025. 123011.

- [34] M.N. Soltani, T. Knudsen, M. Svenstrup, R. Wisniewski, P. Brath, R. Ortega, K. Johnson, Estimation of rotor effective wind speed: A comparison, IEEE Trans. Control Syst. Technol. 21 (4) (2013) 1155–1167.
- [35] K. Chen, J. Yu, Short-term wind speed prediction using an unscented Kalman filter based state-space support vector regression approach, Appl. Energy 113 (2014) 690-705.
- [36] E. Gauterin, P. Kammerer, M. Kühn, H. Schulte, Effective wind speed estimation: Comparison between Kalman filter and Takagi–Sugeno observer techniques, ISA Trans. 62 (2016) 60–72.
- [37] T. Knudsen, T. Bak, M. Soltani, Prediction models for wind speed at turbine locations in a wind farm, Wind. Energy 14 (7) (2011) 877–894.
- [38] N. Abbas, D. Zalkind, L. Pao, A. Wright, A reference open-source controller for fixed and floating offshore wind turbines, Wind. Energy Sci. Discuss. 2021 (2021) 1–33
- [39] W.H. Lio, A. Li, F. Meng, Real-time rotor effective wind speed estimation using Gaussian process regression and Kalman filtering, Renew. Energy 169 (2021) 670–686, http://dx.doi.org/10.1016/j.renene.2021.01.040.
- [40] A. Clifton, D. Schlipf, Wind lidar technology development and transfer, Wind. Energy Sci. 6 (2) (2021) 539–558, http://dx.doi.org/10.5194/wes-6-539-2021.
- [41] A. Visich, B. Conan, Measurement and analysis of high altitude wind profiles over the sea in a coastal zone using a scanning doppler LiDAR: Application to offshore wind energy, Ocean Eng. 325 (2025) 120749, http://dx.doi.org/10. 1016/j.oceaneng.2025.120749.
- [42] H. Wang, Y. Li, J. Yan, W. Xiao, S. Han, Y. Liu, A novel minute-scale prediction method of incoming wind conditions with limited LiDAR data, Renew. Energy 240 (2025) 122235. http://dx.doi.org/10.1016/j.renene.2024.122235.
- [43] I. Miquelez-Madariaga, I. Lizarraga-Zubéldia, A. Diaz de Corcuera, J. Elso, Linear uncertain modelling of LIDAR systems for robust wind turbine control design, Renew. Energy 206 (2023) 367–374, http://dx.doi.org/10.1016/j.renene.2023. 02.062.
- [44] National Renewable Energy Laboratory (NREL), OpenFAST, 2024, National Renewable Energy Laboratory, Software, URL https://openfast.readthedocs.io/.
- [45] F. Angervall, L. Lindenbaum, L. Blom, R. Kristensen, K. Mattsson, O. Hall-berg, Sensorer i chalmers testvindkraftverk: Kalibrering och validering av töjningsgivare i tornet, 2021.
- [46] J.C. Berg, B.R. Resor, Numerical Manufacturing and Design Tool (NuMAD v2. 0) for Wind Turbine Blades: User's Guide, Tech. Rep., Sandia National Laboratories (SNL), Albuquerque, NM, and Livermore, CA (United States), 2012.
- [47] ANSYS, Inc., ANSYS, 2024, ANSYS, Inc., Software, URL https://www.ansys.com/.
- [48] G.S. Bir, User's Guide to PreComp (Pre-Processor for Computing Composite Blade Properties), Tech. Rep., National Renewable Energy Lab.(NREL), Golden, CO (United States), 2005.
- [49] E.A. Bossanyi, The design of closed loop controllers for wind turbines, Wind. Energy: An Int. J. Prog. Applications Wind. Power Convers. Technol. 3 (3) (2000) 149–163.
- [50] European Academy of Wind Energy, Turbine wind tunnel facilities, 2024, https://eawe.eu/site/assets/files/downloads/committees/twtc/TWTC-chalmers-twt-facilities.pdf. (Accessed 22 August 2024).
- [51] T. Hendriksen, B. Bulder, L. Verhoef, DOWEC 6-MW Pre-Design: Aero-elastic Modeling of the DOWEC 6 MW Pre-Design in PHATAS, Tech. Rep. ECN-CX-03-046, Delft University of Technology and Energy Research Centre of the Netherlands (ECN), 2003.
- [52] J. Jonkman, S. Butterfield, W. Musial, G. Scott, Definition of a 5-MW Reference Wind Turbine for Offshore System Development, Tech. Rep., National Renewable Energy Lab.(NREL), Golden, CO (United States), 2009.
- [53] National Instruments, LabVIEW, 2024, National Instruments, Software, URL https://www.ni.com/en-us/shop/labview.html.
- [54] D.J. Laino, A.C. Hansen, User's guide to the wind turbine dynamics aerodynamics computer software AeroDyn, 2002, Salt Lake City, UT: Windward Engineering LLC, Prepared for the National Renewable Energy Laboratory under Subcontract No. TCX-9-29209-01.

- [55] National Instruments, CompactRIO, 2024, National Instruments, Hardware, URL https://www.ni.com/en-us/shop/compactrio.html.
- [56] S. Fogelström, H. Johansson, O. Carlson, M. Hofsäß, O. Bischoff, Y. Marykovskiy, I. Abdallah, Björkö Wind Turbine Version 1 (45kW) High Frequency Structural Health Monitoring (SHM) Data, Zenodo, 2023-08-09, http://dx.doi.org/10.5281/ zenodo.8230330, URL https://zenodo.org/records/8230330.
- [57] S. Fogelström, H. Johansson, O. Carlson, Björkö Wind Turbine Version 1 (45kW) SCADA, Zenodo, 2023-08-01, http://dx.doi.org/10.5281/zenodo.8213270, URL https://zenodo.org/records/8213270.
- [58] F. Angervall, L. Lindenbaum, L. Blom, R. Kristensen, K. Mattsson, O. Hallberg, Sensorer i Chalmers testvindkraftverk: Kalibrering och validering av töjningsgivare i tornet, 2021, arXiv:20.500.12380/303632.
- [59] T. Baba, Time-frequency analysis using short time Fourier transform, Open Acoust. J. 5 (1) (2012) 32–38.
- [60] N.E. Huang, Hilbert-Huang Transform and Its Applications, vol. 16, World Scientific, 2014.
- [61] I. Daubechies, Ten Lectures on Wavelets, SIAM, 1992.
- [62] N.S. Basu Biswajit, C. Arunasis, On-line identification of linear time-varying stiffness of structural system by wavelet analysis, Struct. Heal. Monit. 7 (1) (2008) 21–36.
- [63] T.V.M. Mahato Swarup, C. Arunasis, Adaptive HHT (AHHT) based modal parameter estimation from limited measurements of an RC framed building under multi-component earthquake excitations, J. Struct. Control. Heal. Monit. 22 (7) (2015) 984–1001.
- [64] C.K. Chui, An Introduction to Wavelets, vol. 1, Academic Press, 1992.
- [65] T.V.M. Mahato Swarup, C. Arunasis, Combined wavelet-Hilbert transform based modal identification of road bridge using vehicular excitation, J. Civ. Struct. Heal. Monit. 7 (1) (2017) 29–44.
- [66] M. Swarup, C. Arunasis, Sequential clustering of synchrosqueezed wavelet transform coefficients for efficient modal identification, J. Civ. Struct. Heal. Monit. 9 (2) (2019) 271–291.
- [67] S.C. Olhede, A.T. Walden, Generalized morse wavelets, IEEE Trans. Signal Process. 50 (11) (2002) 2661–2670.
- [68] J.M. Lilly, S.C. Olhede, On the analytic wavelet transform, IEEE Trans. Inform. Theory 56 (8) (2010) 4135–4156.
- [69] J. Lilly, A data analysis package for Matlab, v. 1.6. 2., 2016, http://www.jmlilly.net/imlsoft.html.
- [70] MATLAB, version 9.6.0 (R2019a), The MathWorks Inc., Natick, Massachusetts, 2019a.
- [71] D. Song, J. Yang, M. Dong, Y.H. Joo, Kalman filter-based wind speed estimation for wind turbine control, Int. J. Control. Autom. Syst. 15 (3) (2017) 1089–1096, http://dx.doi.org/10.1007/s12555-016-0537-1.
- [72] W.H. Lio, A. Li, F. Meng, Real-time rotor effective wind speed estimation using Gaussian process regression and Kalman filtering, Renew. Energy 169 (2021) 670–686, http://dx.doi.org/10.1016/j.renene.2021.01.040.
- [73] D. Song, J. Yang, Z. Cai, M. Dong, M. Su, Y. Wang, Wind estimation with a non-standard extended Kalman filter and its application on maximum power extraction for variable speed wind turbines, Appl. Energy 190 (2017) 670–685, http://dx.doi.org/10.1016/j.apenergy.2016.12.132.
- [74] IEC-61400-3, Wind turbines Part 3: Design requirements for offshore wind turbines, 2009, International Electrotechnical Commission.
- [75] A. Platt, B. Jonkman, J. Jonkman, InflowWind User's Guide, Technical Report, 2016.
- [76] Y. Bar-Shalom, X.-R. Li, T. Kirubarajan, Estimation, Tracking and Navigation: Theory, Algorithms and Software, Wiley, 2001.
- [77] B.J. Jonkman, TurbSim user's guide: Version 1.50, Tech. Rep., National Renewable Energy Laboratory (NREL), Golden, CO (United States), 2009.
- [78] Chalmers Wind Turbine, 2024, https://www.chalmers.se/en/departments/e2/ resources-and-collaboration/chalmers-wind-turbine/.
- [79] Test Wind Turbines Committee | Pioneering Wind Turbine Testing, 2025, EAWE, https://eawe.eu/committee/eawe-windeurope-scientific-track-west-committee/.